Published in final edited form as:
Neuroimage. 2009 July 15; 46(4): 1091–1104. doi:10.1016/j.neuroimage.2009.03.026.

Reward Circuitry is Perturbed in the Absence of the Serotonin Transporter

Elaine L. Bearer[1,2], **Xiaowei Zhang**[1], **Davit Janvelyan**[1], **Benoit Boulat**[1], and **Russell E. Jacobs**[1]

1 *Biological Imaging Center, Beckman Institute, California Institute of Technology, Pasadena, CA 91125*

2 *Department of Pathology and Laboratory Medicine, Brown University, Providence, RI 02906*

Abstract

The serotonin transporter (SERT) modulates the entire serotonergic system in the brain and influences both the dopaminergic and norepinephrinergic systems. These three systems are intimately involved in normal physiological functioning of the brain and implicated in numerous pathological conditions. Here we use high-resolution magnetic resonance imaging (MRI) and spectroscopy to elucidate the effects of disruption of the serotonin transporter in an animal model system: the SERT knock-out mouse. Employing manganese-enhanced MRI, we injected Mn^{2+} into the prefrontal cortex and obtained 3D MR images at specific time points in cohorts of SERT and normal mice. Statistical analysis of co-registered datasets demonstrated that active circuitry originating in the prefrontal cortex in the SERT knock-out is dramatically altered, with a bias towards more posterior areas (substantia nigra, ventral tegmental area, and Raphé nuclei) directly involved in the reward circuit. Injection site and tracing were confirmed with traditional track tracers by optical microscopy. In contrast, metabolite levels were essentially normal in the SERT knock-out by in vivo magnetic resonance spectroscopy and little or no anatomical differences between SERT knock-out and normal mice were detected by MRI. These findings point to modulation of the limbic cortical-ventral striatopallidal by disruption of SERT function. Thus, molecular disruptions of SERT that produce behavioral changes also alter the functional anatomy of the reward circuitry in which all the monoamine systems are involved.

Keywords

serotonin transporter; knock-out; manganese enhanced MRI; synaptic transmission; transport; morphometry; statistical parametric mapping; DTI; MRS

Introduction

The serotonin transporter (SERT) regulates serotonin levels in the synaptic cleft through active uptake from the extracellular space (Li, 2006) and is encoded by a single gene in mouse (Bengel et al., 1997). SERT is the target of a large class of psychoactive drugs used in a number of anxiety disorders, as well as drugs of abuse such as cocaine and

Corresponding author: Russell E. Jacobs, PhD, m/c 139-74 Caltech, 1200 E. California Blvd, Pasadena, CA 91125-7400, Phone (626) 395-2849, FAX (626) 449-5163, Email E-mail: rjacobs@caltech.edu.

methylenedioxymethamphetamine (MDMA). Moreover, SERT is the principal regulator of the entire serotonergic system (Murphy et al., 2004) and dysregulation of SERT gene expression is implicated as a risk factor for a number of affective disorders (Gainetdinov and Caron, 2003;Murphy et al., 2004;Murphy et al., 2001).

Mouse knock-outs for SERT and the other two monoamine transporters, dopamine transporter (DAT) and norepinephrine transporter (NET), have been used extensively to study the pharmacological, behavioral, and anatomic consequences of disruption (Caron, 1999; Dykstra et al., 2003; Gainetdinov and Caron, 2003; Gainetdinov et al., 2002; Hall et al., 2004; Kita et al., 2003; Numachi et al., 2007; Reith, 2005; Rocha, 2003; Torres and Caron, 2005; Uhl, 2003; Uhl et al., 2002; Xu et al., 2000; Yamashita et al., 2006). Single and multiple knock-outs of the monoamine transporters have been especially useful in investigations aimed at linking the molecular actions and behavioral consequences of drugs of abuse (Sora et al., 2001; Uhl and Lin, 2003). These studies have generated a wealth of information about specific aspects of these model systems at the molecular level (*e.g.* up/down regulation of monoamine receptors in response to uptake inhibition, altered concentrations of monoamine metabolites and related molecules), and at the behavioral level (*e.g.* conditioned place preference, locomotor response, drug induced response) (Homberg et al., 2007; Li et al., 2003; Numachi et al., 2007; Rocha, 2003; Shen et al., 2004).

Here we explore brain circuitry in SERT knock-out mice to link molecular alterations to anatomical and behavioral observations. SERT knock-out mice exhibit avoidance and hyperarousal and are more vulnerable to stress than wild-type mice (Adamec et al. 2008). In addition, SERT mice display an initial impairment of food- and cocaine-self-administration (Thomsen et al. 2009). A number of behaviors, including addiction, anxiety, aggression, and affective disorders such as depression, have been linked to anatomical brain regions, specifically the limbic cortical-ventral striatopallidal circuitry (Berton and Nestler, 2006; Everitt and Robbins, 2005; Murphy and Lesch, 2008; Nelson and Trainor, 2007; Robbins and Everitt, 2002). The prefrontal cortex (PFC) is believed to perform executive functions in this circuit (Berton and Nestler, 2006; Robbins and Everitt, 2002) where it has been implicated in working memory, affect, temperament, attention, response initiation and management of autonomic control and emotion (Canli et al., 2001; Groenewegen and Uylings, 2000; Groenewegen et al., 1997; Hagen et al., 2002; Zald et al., 2002). The PFC is also densely innervated by serotonergic neurons arising in the median Raphe nuclei of the brain stem (Puig et al., 2004). Recent work in monkey demonstrates that injection of Mn^{2+} into the PFC traces expected pathways deeper into the brain (Simmons et al., 2008). How these pathways might be altered by a loss of SERT activity remains an open question.

Due to the importance of the PFC and its connections, and the expected involvement of serotonin in this circuit, we chose to exploit the SERT knock-out mouse to probe circuitry originating in the PFC with and without SERT activity. After stereotaxic injection of nanoliter volumes of $MnCl_2$ into the PFC of knock-out and normal control mice, we followed the time course of Mn^{2+} uptake, transport, and accumulation over the first 24 hours post injection by sequential high resolution MRI. We also employed MRS to compare metabolite levels in living brains of normal versus SERT knock-out mice. After *in vivo* MR imaging, we fixed the brains and used diffusion tensor imaging to obtain additional structural information and then processed them for histology and analysis by microscopy. Co-injection of fluorescent tracer with the Mn^{2+} allowed definitive identification of the injection site, confirming its location and lack of damage at the cellular level. Detection of this conventional fluorescent tracer at distant sites was examined to verify the MEMRI results.

Finally, we adopted a non-biased comprehensive approach to identify all connections traced by Mn^{2+} throughout the brain after PFC injection. Whole brain MRI data sets from both

genotypes at all time points were co-registered into the same 3D space (Kovacevic et al., 2005; Lee et al., 2005) using a straightforward linear and nonlinear alignment (Bearer et al., 2007b; Tyszka et al., 2006). Image alignment allows an automated voxel-wise comparison of 3D MR images (Hammers et al., 2003; Kassubek et al., 2004; Lee et al., 2005; Mechelli et al., 2005; Toga and Mazziotta, 2002). This allows identification of those voxels with statistically significant intensity changes across time and between cohorts (Bearer et al., 2007b; Cross et al., 2004). By comparing the intensities between one time point and the next, we detected the pathway of the Mn^{2+} as it progressed along neuronal circuits in each genotype. This allowed us to probe changes in the reward/addiction circuitry (limbic cortical-ventral striatopallidal) due to loss of SERT activity.

Materials and Methods

Animals

Mice were obtained from Taconic Farms, Inc (Hudson, NY). Ten serotonin transporter (SERT) knock-out mice (Taconic: B6.129-Slc6a4^{tm1Kpl} N_{10}) and ten normal mice (C57Bl/6NTac) were used in this study. Mice were female between the ages of 19 and 23 weeks. All experiments were performed in accordance with protocols approved by the Institutional Animal Care and Use Committee of the California Institute of Technology.

Stereotaxic Injections

Stereotaxic injection procedure was similar to that employed by Bearer et al (Bearer et al., 2007b). Mice were anesthetized by spontaneous inhalation of 1% isoflurane and placed in a stereotaxic frame (Kopf Instruments, Tujunga, CA). 5nl of 600mM $MnCl_2$ with 0.5 mg/ml 3k rhodamine dextran-amine (RDA) (Molecular Probes/Invitrogen, Eugene, OR) was injected unilaterally into the right prefrontal cortex (coordinates x −0.5 mm (lateral), y 1.0 mm (anterior-posterior A–P with bregma=0), z 1.0 mm (dorso-ventral D–V with brain surface=0) (Paxinos and Franklin, 2001)) over 5 minutes using a quartz micropipette (1mm OD quartz capillary pulled to approximately 80μm OD tip). The animal then received 0.2ml glycopyrrolate (0.02 mg/kg) and 0.1ml dextrose (5%) subcutaneously; with 0.2ml lactated Ringer's solution (10ml/kg) IP. It was then immediately placed in the MR scanner under 0.8% isoflurane anesthetic.

Preparation for ex vivo imaging

From 1 to 10 days after *in vivo* imaging, animals were sacrificed and brains fixed via transcardiac perfusion with 4% paraformaldehyde (PFA) as previously described (Tyszka et al., 2006). After overnight rocking in 4% PFA at 4°C the mouse head was cleaned of skin, lower jaw, ears and cartilaginous nose tip and then rocked in 50ml 0.01% sodium azide in PBS for 7 days at 4°C. The head was then transferred to a 5mM solution of gadoteridol (Prohance®, Bracco Diagnostics Inc, Princeton NJ) and 0.01% sodium azide in PBS and rocked for 7 days at 4°C prior to MR imaging.

Magnetic Resonance Imaging and spectroscopy

Each animal was scanned before the stereotaxic injection; and beginning at 0:38±0:14, 1:20 ±0:14, 2:00±0:16, 2:44±0:14, 4:08±0:14, and 22:51±1:02 hours post injection. Times are averages over all animals ± standard deviation. We use the midpoint of each 40 minute scan as the "scan time" and for convenience call these the 1hr, 1hr40m, 2hr20m, 3hr, 4hr20m and 24hr time points. An 11.7T 89mm vertical bore Bruker BioSpin Avance DRX500 scanner (Bruker BioSpin Inc, Billerica, MA) equipped with a Micro2.5 gradient system was used to acquire all mouse brain images and spectroscopic data with a 35mm linear birdcage RF coil. For *in vivo* imaging the animal's head was secured in a Teflon stereotaxic unit within the RF coil to minimize movement and aid in reproducible placement. Temperature and respiration

were continuously monitored during data acquisition and remained within normal ranges. We employed a 3D RARE imaging sequence (Hennig et al., 1986) with RARE factor of 4, 4 averages, TR/TE_{eff} = 250ms/24ms; matrix size of 160×128×78; FOV 16mm × 12.8mm × 7.8mm; yielding 100μm isotropic voxels with 40 minute scan time. The short TR provides T_1 weighting to emphasize the location of the paramagnetic Mn^{2+}, while the relatively long effective TE (24ms) provides T_2 weighting that aids in providing contrast between different anatomical features.

All *in vivo* mouse brain magnetic resonance spectroscopy (MRS) experiments were conducted using Point Resolved Spectroscopy (PRESS) (Bottomley, 1987) with a short echo time TE of 7.267 milliseconds, recycle time of 2.3 seconds, a spectral width of 7KHz, 4000 data points in each free induction decay signal (FID), and 128 averages. The sequence was preceded by a VAPOR water suppression module (Tkáč et al., 1999) interleaved with outer volume saturation. Optimized second order shimming was done with the Fastmap routine (Gruetter, 1993) in a 5 mm cube centered in the striatum. The PRESS spectra were then recorded inside a $2mm^3$ volume (8 μl) at the center of the volume used for shimming.

For *ex vivo* imaging, two intact fixed heads were secured in a Teflon® holder and submerged in a perfluoropolyether (Fomblin®, Solvay Solexis, Inc, Thorofare, NJ) within a 50ml vial and imaged. The ambient bore temperature was maintained at 4°C by thermostatically controlled airflow. Diffusion weighted images were acquired using a conventional pulsed-gradient spin echo (PGSE) sequence (TR/TE = 300ms/11.9ms, 256 × 150 × 120 matrix, 25.6mm × 15mm × 12mm FOV, 100μm isotropic voxel size, 1 average, δ = 3ms, Δ = 5.2ms, Gd = 1125mT/m, nominal b-factor = 3370 s/mm^2). An optimized six point icosahedral encoding scheme (Hasan et al., 2001) was used for diffusion weighted acquisitions with a single un-weighted reference image for a total imaging time of 14.5 hours.

Histology

Brains were fixed in pairs (SERT/normal) at different time points (1, 2, 4, 6, 8, 11, 12, 13, 16 and 21d) after injection to allow histologic determination of transport differences. After fixation and *ex vivo* MR imaging, brains were dissected from the calvarium and sent to Neuroscience Associates (NSA, Knoxville, TN) for gelatin embedding and serially sectioned coronally at 30–35 μm. All 20 brains were embedded in register into the same gelatin block, allowing review of the same location in the entire set on one microscope slide. Sections were collected into 24 cups sequentially, such that each cup contained every 24th section spanning the whole brain of all 20 individuals. Alternate cups were selected for staining with either Thionine/Nissl for cellular morphology, or for mounting unstained in anti-quench with DAPI (Vector Lab, Burlingame, CA) to image the RDA fluorescence. Sections were imaged on a Zeiss AxioImager Z1 equipped with both hallogen and mercury illumination, He43 filter cube, and 5x, 10x, 20x, 40x, 63x and 100x neofluor objectives, Images were captured by an Axiocam HRC or MRM using AxioVision 4.5 software.

Image Alignment and Statistical Parametric Mapping

Pre and post Mn^{2+} injection MR images were skull-stripped using the Brain Surface Extractor (BSE) within BrainSuite 2 (Shattuck and Leahy, 2001) to remove all non-brain material. Inaccuracies were corrected by manually editing the masks using BrainSuite 2. After skull stripping, field inhomogeneities were corrected using the N3 method (Sled et al., 1998) and each was scaled to the mode of its intensity histogram (Bearer et al., 2007b; Kovacevic et al., 2005). A minimum deformation target (MDT) was produced as described (Kochunov et al., 2001). Briefly, all pre-injection images were aligned to a representative individual with a 12-parameter full-affine transformation using Alignlinear (AIR 5.2.5) (Woods et al., 1998a; Woods et al., 1998b) with the least squares with intensity rescaling cost function. The resulting

transformations were averaged and all pre-injection images were aligned to the average with a 12-parameter full-affine model. The resulting transformations for each cohort were averaged and the pre-injection images were then warped into this MDT common space beginning with a 2^{nd} order 30 parameter model and ending with a 5^{th} order 168 parameter model using Align_warp (AIR 5.2.5). For each sample, the post injection images were linearly aligned (12 parameter model) to the pre-injection image using Alignlinear, followed by the polynomial warp field used to transform that sample's pre-injection image into the MDT. All automated image processing was performed in the LONI Pipeline Processing Environment (Rex et al., 2003) using either a 32-processor Onyx 200 or 64-processor Origin 3000 supercomputer (SGI). This process placed all the images in the same space so that voxel-wise comparisons could be made among the different data sets. Final images were blurred with a 0.3mm Gaussian kernel and a paired Student's t-test, as implemented in SPM5 (Wellcome Trust Centre for Neuroimaging, University College London), was used to determine which voxels increased in intensity when comparing one time point to the next. Similar processing was used to compare rotationally invariant indices derived from DTI datasets, except that an unpaired Student's t-test was used to compare knock-out and normal cohorts. Parametric maps of voxels with statistically significant changes in intensity were created to display the results and to correlate increases with underlying anatomy (Bearer et al., 2007b). Anatomy was determined with reference to Hoff et al (Hof et al., 2000) and the Allen Brain Atlas (Dong, 2008) (http://www.brain-map.org/welcome.do). Sagittal sections were typically more helpful than coronal in identifying and comparing anatomical structures in the in vivo MR images.

Tensor Based Morphometry

A deformation field analysis implemented by Thompson and coworkers (Lepore et al., 2008) was used to analyze whether MRI scans of the SERT knock-out differ anatomically from normal mouse brain scans. This approach has been used previously in studies of both mouse (Kovacevic et al., 2005; Ma et al., 2005; Spring et al., 2007; Verma et al., 2005) and human (Lepore et al., 2008; May and Gaser, 2006; Perani et al., 2005; Reading et al., 2005). Briefly, all scans of a particular contrast (*e.g.* pre-injection, iDWI) were mapped into an MDT. The resulting displacement field (J^TJ, with J the deformation Jacobian) for each scan was employed in the actual analysis. Maps of the determinant of J^TJ were used in a voxel-wise Hotteling's T^2 test yielding p-value maps to gauge statistical differences between the two cohorts at each voxel in the image.

Determination of relative metabolite concentrations

For each mouse brain the spectrum of the relative amount of metabolites inside the experimental PRESS volume was quantified using the QUEST (quantitation based on quantum estimation) module (Ratiney et al., 2005) available inside the Java Magnetic Resonance User Interface (JMRUI) package (Naressi et al., 2001). A basis set comprising nine metabolites was used to perform the fit. To this end PRESS spectra of creatine, choline, N-acetyl aspartate (NAA), taurine, myo-inositol, lactate, glutamine, glutamate and gamma-amino-butyric acid (GABA) were simulated using the NMR-SCOPE (Graveron-Demilly et al., 1993) simulation package within JMRUI. The spin parameters (number of spins, chemical shifts, J-couplings) were obtained from Govindaraju (Govindaraju et al., 2000). The choice to use a simulated basis set rather than a measured one was based on recent results showing no statistically significant differences between estimates obtained using either basis set (Cudalbu et al., 2007). Metabolite amounts obtained by the QUEST were normalized to creatine.

Diffusion tensor image construction

Reconstruction of the apparent diffusion-weighted images included spatial radial Gaussian filtering (0.25 voxel width) to smooth the co-registration cost-function and improve the SNr

of all subsequent calculations. The apparent diffusion tensor was calculated conventionally by inversion of the encoding b-matrix. The b-matrix for each diffusion encoding was determined by numerical simulation of the pulse sequence k-space trajectory in order to account for gradient cross-terms (Mattiello et al., 1997). Eigenvalues, eigenvectors, tensor trace and fractional anisotropy were calculated conventionally using built-in and custom Matlab functions (The Mathworks Inc., Natick MA). The six diffusion weighted images were averaged to generate a high SNr isotropic diffusion weighted image (iDWI). Diffusion tensor images (and associated images of eigenvalue, λ_i; trace, Tr(**D**); and fractional anisotropy, FA) were placed into the same space for voxel-wise comparisons using the methods outlined above for in vivo MR images.

Rendering

Visualization of the MR images and statistical parametric maps was performed with ResolveRT4 (Mercury Computer Systems, Inc., Hudson, NH) and MRIcro (Rorden and Brett, 2000).

Results

Injection site location and condition

The injection sites were within a 0.3 mm radius for all 20 animals, as demonstrated in MR images recorded 1 hour after Mn^{2+} injection into the PFC (Figure 1). The average injection site for all 20 animals was: x (lateral) +0.45±0.16mm, y (A–P), +0.92±0.28mm, z (D–V) −0.86 ±0.27mm; for the SERT knockouts: x +0.43±0.16mm, y +0.74±0.25mm, z −0.83±0.26mm; and for the normals: x +0.47±0.17mm, y +1.1±0.18mm, z −0.88±0.29mm. Co-injection of fluorescent dextran allowed identification of the injection site by histology. We therefore performed a comprehensive histological analysis of all 20 brains to verify the location of the injection site, detect any morphologic evidence of injury, and validate that the injectate was delivered into the pathway previously identified by traditional tracers (Gabbott et al., 2005;Sesack and Pickel, 1992). The injection site could only be identified in 8 of 20 brains (4 normals and 4 SERT) that were fixed at 1–8 days after injection. At later time points, the injection site could not be identified. In 4 of the 20 brains, the injection site was only identifiable by the presence of fluorescent dextran as no other sign could be found in our serial histologic sections, whether stained for morphology with DAPI or with Nissl/Thionine (Figure 2). Nor could any gliosis, an indicator of brain injury, be found at later time points (Figure 2). In those brains where the injection site was identified by the presence of rhodamine-dextran, the surrounding tissue showed no increased cellularity, evidence of bleeding, or other damage/ injury response, although the injectate did appear as a small droplet (50–100 μm diameter) displacing brain tissue at 1 day post injection. The location of identified injection sites in the PFC matched the injection position in MR images.

In both SERT knock-out and normal mice microscopic examination of locations distant from the injection site showed a significant number of rhodamine positive cells. These areas were restricted to regions representing predicted targets in the pathway from PFC, such as the globus pallidus (Figure 3).

Metabolite concentrations are similar in SERT and wild-type mice

In vivo magnetic resonance spectroscopy offers a means to monitor non-invasively low molecular weight metabolite levels within the intact brain (Choi et al., 2003; Jansen et al., 2006; Maudsley, 2002; Tkac et al., 2004). In this study we determined concentrations of metabolites relative to creatine, which is assumed to remain constant among mice and between the two cohorts (Figure 4). All spectra were recorded from a $2mm^3$ volume centered in the striatum (Figure 4B). Although Student's t-test statistical comparisons between the metabolite

levels from the SERT knock-out and normal cohorts indicate that none of the metabolites are statistically different at a $p<0.05$ level, the choline and taurine levels are different at $p<0.053$; both being larger in the SERT knock-out versus normals.

Voxelwise Analysis detects no anatomical differences in SERT compared to normal mice

We aligned 3D MR images of 20 living mice, 10 for each genotype, into a single 3D atlas and used statistical parametric mapping to compare brain structure between genotypes. Two separate statistical analyses were performed. In the first, the extent of anatomical morphometric alterations undergone by the SERT knock-out was determined by tensor-based morphometry (TBM) of both *in vivo* and fixed MRI data sets. Secondly, the impact of SERT knock-out on tissue structure manifest in altered water diffusional characteristic was determined by image alignment and statistical parametric mapping of images of FA and Tr(D) (Verma et al., 2005).

The TBM analysis revealed that both the pre-injection *in vivo* scans and iDWI *ex vivo* scans had an extremely small number (less than 0.1% of the brain volume) of statistically different ($p<0.01$) voxels randomly scattered about the brain (colored areas in Figure 5). For the TBM analysis all the pre-injection data sets were mapped to the same MDT, the Jacobian of the deformation field calculated, and p-value maps noting statistical significance of differences in the deformations of the two cohorts determined. A similar calculation was done beginning with the iDWI data sets measured on fixed brains. In Figure 5 green areas denote voxels that differ significantly between the SERT knock-out and normal mouse brain scans at $p<0.01$.

After warping into the same space, an unpaired Student's t-test was used to gauge whether the normal and SERT knock-out have different patterns of FA or Tr(D). No patterns of differences were observed with either FA or Tr(D) measurements with very few significantly different voxels between the brains of SERT knock-out and normal mice: 0.4% for FA and 0.2% for Tr (D) (Figure 6). Colored voxels show the differences between the SERT knock-out and normal mouse at a significance level of $p<0.01$.

Visualization of Mn^{2+} transport in the limbic system of living mice

In contrast to the results of spectroscopy and DTI imaging, where little to no differences between SERT knock-out and normal mice were found, Mn^{2+} accumulation over time was profoundly different in SERT knock-outs compared to normals. Alignment and a consistent intensity scaling allowed us to visually and computationally follow the changes due to the appearance of Mn^{2+} induced hyperintensity in structures distant from the injection site in averaged co-aligned images, such as the slices shown in Figure 7. We aligned all of the SERT knock-out *in vivo* MR images, then at each time point averaged the images from the 10 individual SERT knock-out mice. The averaged images preserve the fidelity of the original images – anatomical structures are clear and distinct (*e.g.* ventricles, corpus callosum, hippocampus, internal and external capsule are all easily identifiable) (Figure 7). Signal intensities in the globus pallidus (GP) and substantia nigra (SNr) regions are qualitatively unchanged from pre-injection to the 3 hour time point, then increase at 4 hours and increase again at 24 hours (Figure 7A). Intensity measurements in a region of interest (ROI) within the GP ipsilateral to the injection site as a function of time after injection in averaged images from each time point and genotype confirm the visual assessment (Figure 7B)

Statistical mapping of Mn^{2+} tracing from PFC injection: Profound differences between SERT knock-out and normal mice

For an unbiased assessment of the whole brain, we performed automated voxel-wise statistical parametric mapping to determine the spatial extent of Mn^{2+} accumulation as a function of time after injection (Figure 8 and Supplemental Data). For clarity, normal and SERT knock-out

cohorts are shown separately, and volumes with significant increases ($p<0.025$) are color coded. Comparisons between the earliest two time periods are shown in pure green for both the SERT knock-out and normal animals, while later times are displayed with increasing amounts of blue for the SERT knock-out and red for the normal animal.

The injection site was readily detected in the 1hr compared to pre-injection statistical map, as shown in green in Figure 8. The pure green colored regions are voxels that are significantly more intense immediately post injection than before injection of a small amount of Mn^{2+} into the prefrontal cortex. As the green areas (1hr>pre) show in slice 1 of the coronal view (Figure 8A and 8B) and slices 3–5 of the sagittal view (Figure 8C and 8D), after the injection a spheroid of hyperintensity in the MR image appears, likely due to Mn^{2+} diffusion. Comparison of the 1hr40m image data sets with those recorded at 1hr post-injection reveals no significant changes in either the SERT knock-outs or normal animals.

By 2hr20m post-injection, Mn^{2+}-induced intensity changes had already progressed from the injection point to more distal locations. Wide spread changes were already apparent at 2hr20m post injection between the two genotypes. (Figure 8. 2hr20m>1hr40m). For the SERT knockouts, at the most dorsal level of the injection site on the ipsilateral side only, the hyperintensity increase expands outward through layers 3 and 4 of the cortex (blue-green regions in Figure 8B slices 1 and 2, Figure 8D slices 1–3). At 1.5mm off midline, the hyperintensity increase dips into the dorsal anterior portion of the caudate putamen (CP), courses across the CP and down into the globus pallidus (GP), bed nucleus of the stria terminalis (BST), and most rostral portion of the thalamus (TH). These changes are especially apparent in the ipsilateral sagittal slices (Figure 8D slices 1–5). For the normal animals, we see relatively small isolated volumes of hyperintensity increase in the CP ipsilateral to the injection site and just outside the injection volume on the contralateral side (Figure 8A slice 1; Figure 8C slices 2, 7, 8).

From 2hr20m to 3 hours post-injection, the SERT knock-outs show additional hyperintensity increase in the ipsilateral CP; spreading ipsilateral to contralateral in a discontinuous arc through several nuclei of the anterior TH (Figure 8B slices 2–4). For the normal cohort, we note hyperintensity increase dorsal to ventral across the anterior third of the ipsilateral CP, connecting to the medial edge of the CP and down through the BST with a small amount in the paraventricular TH; and hyperintensity increase contralateral in the dorsal and mid level CP, medial portion of the GP, and more ventrally in the BST with small amounts in the TH and the nucleus accumbens (ACB). See Figure 8A slices 3–5 and Figure 8C slices 1–4.

From 3 hours to 4hr20m post-injection, the SERT knock-outs have additional hyperintensity increase with more volume occupied in the same locations as 3hr>2hr20m statistical parametric map (SPM). The arc through the TH is now broader and continuous to the contralateral GP. For the normal animals, hyperintensity increases are displayed in major portions of the ipsilateral CP and medial portions of the GP, leading down to the BST, then into the reticular nucleus (RT) and central portions of the TH with additional intensity increases in dorsal regions of the hypothalamus (HY). No changes are seen contralateral to the injection site in this comparison (Figure 8. 4hr20m>3hr).

Major differences in the accumulation of Mn^{2+} signal evolved throughout the time course of the experiment in both cohorts. The extent and location of these changes become increasingly different between the two cohorts over time. Between 4hr20m and 24 hours, widespread changes were seen in images from both knock-out and normal cohorts (pure red and blue in Figure 8).

In the normal animals, three significant threads of hyperintensity can be identified, with none extending further posterior than the TH at −2.5mm Bregma. One thread runs from Layer 5

cortex at 0.5mm Bregma tracing diagonally back to the midline at −1.6mm Bregma in the retrospinal cortex (Figure 8A slices 2–4). The second thread is ipsilateral to the injection site filling much of the CP, and large portions of the GP, ACB, and substantia innominata (SI); plus the claustrum (CLA) and nearby cortex. This thread further expands to fill half the TH farthest from the midline (Figure 8A slices 4 and 5, 8C slices 1 and 2). The third thread is contralateral to the injection site and somewhat smaller than the second thread but occupies substantially the same anatomy (Figure 8A slices 4 and 5, Figure 8C slice 8 and 9).

In the SERT knock-outs by 24 hr, three distinct differences with normals become obvious. First, instead of distinct threads progressing from the injection site, in the knock-outs we note a more general spread of the hyperintensity posterior to the mid level TH with a larger volume occupied contiguously across the entire TH, *i.e.* compare the 24hr>4hr30m SPM with the 4hr20m>3hr SPM (Figure 8B slice 5). Second, the enhanced region extends more ventrally to occupy much of the substantia nigra (SNr) both ipsilateral and contralateral to the injection site (Figure 8B slices 6 and 7, Figure 8D slices 2 and 3), as well as the ipsilateral ventral tegmental area (VTA) (Figure 8B slice 8, Figure 8D slice 4). Finally, significant intensity increases are observed far posterior into the dorsal nucleus Raphé (DNR), red nucleus (RN) and pontine reticular nucleus (PRN) (Figure 8B slices 9–12, Figure 8D slices 3–5). This accumulation of Mn^{2+} in the posterior regions of the brain was not detected in normals.

Discussion

Here we show profound differences in the neuronal circuitry caused by a genetic disruption of the serotonin transporter in a mouse model system using a panel of magnetic resonance methods. Both metabolite detection by MRS and anatomy by TBM and DTI demonstrated no detectible differences between SERT knock-out and normal mice. In contrast, widespread differences were revealed by neuronal transport of the MR contrast agent, Mn^{2+}. After injection of Mn^{2+} into the prefrontal cortex of living mice, the classic pathway to the limbic system became highlighted over 24 hours in normal mice, whereas in SERT knock-out, Mn^{2+}-induced increased intensity occurred more caudally, progressing into the dorsal nuclei Raphé of the brain stem. Thus by 24 hours little overlap in the highlighted anatomy between the two types of mice was found. This dramatic difference in Mn^{2+} accumulation cannot be explained by alterations in metabolite levels or anatomy of the mutants.

MRS detectable metabolite levels in the caudate putamen of knock-out mice are similar to normals. Thus neuronal viability (indicated by NAA/Cr), excitatory and inhibitory system integrity (indicated by Glu/Cr and GABA/Cr), membrane turnover (indicated by Cho/Cr), and glial volume (indicated by Tau/Cr) are not significantly different between the SERT knock-out and normal animal (Brian Ross, 2001; Dedeoglu et al., 2004; Hetherington et al., 1997; Lyoo and Renshaw, 2002; Marjanska et al., 2005; Morris, 1999; Rothman et al., 2003; Rudin et al., 1995).

Histology also demonstrated no detectible toxic effect of the injectate containing 3 nmol of Mn^{2+} on the brain parenchyma in either genotype. This agrees with work of Canals and coworkers who found a threshold for neuronal cell death of 16nmol and for astrogliosis of 8nmol Mn^{2+} (Canals et al., 2008). Thus differences in MEMRI delineated pathways are not due to selective anatomical damage by the injection in either genotype.

Tensor-based morphometry (TBM) also failed to show any gross anatomical differences between the two cohorts, *i.e.* no differences in the size or shape of structures, no missing structures, no cerebellar or hippocampal dysmorphism. We used TBM to compare the SERT knock-out and the normal mouse brain based on *in vivo* pre-injection MRI and *ex vivo* iDWI data sets. Thus, the lack of change must be viewed within the context of the limited spatial

resolution (100μm) and contrast of the images. Histological examinations reveal that SERT knock-out mice have altered barrel field morphology (Persico et al., 2001) and other cellular level changes in the cortex and other parts of the brain (Altamura et al., 2007; Li, 2006; Persico et al., 2000a; Wellman et al., 2007). The TBM methodology as implemented here is insensitive to changes at the higher resolution used to detect these microscopic anatomical differences.

Fractional anisotropy (FA) and the trace of the water diffusion tensor (Tr(D)) have been used to gain insight into changes in white matter tracts and other ordered brain structures (Drobyshevsky et al., 2005; Tyszka et al., 2006; Wieshmann et al., 1999). FA and Tr(D) are two rotationally invariant indices derived from the diffusion tensor that provide information about underlying tissue characteristics (Alexander et al., 2001; Basser, 1995; LeBihan, 1995; Mori et al., 2001; Papadakis et al., 1999; Pfefferbaum et al., 2000; Song et al., 2002; van Doorn et al., 1996). Fractional anisotropy is a scalar measure of the diffusion anisotropy (*i.e.* propensity of water to diffuse along, rather than perpendicular to, nerve bundles). Tr(D) is a measure of the orientation-independent mean diffusivity of water in the tissue. Statistical parametric maps of our data failed to detect any meaningful differences between FA and Tr (D) datasets from SERT knock-out and normal mice. Hence the tracts and ordered structures detected by FA and Tr(D) are essentially normal in the SERT knock-out. Thus, anatomical differences at the 100μm resolution of this data are unlikely to contribute to the large differences in Mn^{2+} distribution.

The dramatic differences in Mn^{2+} enhanced MR images in the SERT knock-out mice compared to normal animals were found both in the anatomical distribution of Mn^{2+}-induced intensity increases and in the time course of their appearance. After introduction of nanoliter amounts of Mn^{2+} into the prefrontal cortex, both knock-out and normal mice displayed Mn^{2+} accumulation in the CP, GP, and thalamus; while only the knock-out showed additional accumulation further basal and posterior in the hypothalamus, SNr, VTA, RN, and PRNr over time.

Mn^{2+} is an anterograde trans-synaptic tracer thought to be selectively taken up through Ca^{2+} or other divalent cation channels and transported via fast axonal transport within neurons to accumulate at distant sites in sufficient amounts to produce significant intensity changes detected by T_1-weighted MRI (Murayama et al., 2006; Silva et al., 2004; Van der Linden et al., 2007). Moreover, Mn^{2+} is an activity dependent tracer, as it is taken up by active neurons via voltage gated Ca^{2+} channels (Aoki et al., 2002; Drapeau and Nachshen, 1984; Narita et al., 1990) and crosses active synapses (Bearer et al., 2007a; Pautler et al., 2003; Saleem et al., 2002). There is no known specificity of Mn^{2+} for any particular type of neuron. Thus, the projections observed in this work likely arise from all neurons at the forebrain injection site, regardless of their neurotransmitter specificity. In this regard, several cellular level differences in the prefrontal cortex have been observed between SERT knockout and normal mice, including increased neuronal density, changes in layer thickness, and increased branch length in pyramidal neuron dendrites (Altamura et al., 2007; Persico et al., 2003; Persico et al., 2001; Wellman et al., 2007). These cellular differences must modulate to some extent the initial uptake and, thus, could modulate the temporal distribution of Mn^{2+} originating in the forebrain. Cellular differences due to SERT knock-out have also been noted in locations such as the somatosensory cortex, amygdala, hypothalamus, striatum, and dorsal Raphe (Kim et al., 2005; Li, 2006; Li et al., 2003; Lira et al., 2003; Persico, 2004; Persico et al., 2000b; Wellman et al., 2007). These structural, cellular, and molecular differences all contribute to the functional differences in neuronal circuits in the two cohorts of mice that affect the transport/relocation of Mn^{2+}. This interpretation is consistent with other studies of SERT knock-out mice showing that they exhibit significant adaptive changes at the molecular/synaptic/cellular level; including region specific changes in various serotonin receptor densities and altered responses in other

neurotransmitter systems (Fox et al., 2007; Kim et al., 2005; Li, 2006; Murphy et al., 2004; Murphy and Lesch, 2008; Shen et al., 2004; Wellman et al., 2007).

Mn^{2+} transport in the normal animal delineates some, but not all, of the expected connections between the neocortex and the basal ganglia of the rodent brain (Carr and Sesack, 2000; Gabbott et al., 2005; Paxinos, 2004). Over the course of 3 hours, Mn^{2+} is transported from the prefrontal cortex to the caudate putamen (CP) and then onto the globus pallidus (GP), nucleus accumbens (ACB), and thalamus (TH). Similar connections were observed in the rat after stereotaxic injection on Mn^{2+} into the CP (Soria et al., 2008). By 4 hours post-injection hyperintensity is seen in the bed nucleus of the stria terminalis (BST) and dorsal regions of the hypothalamus (HY). We interpret the large volume of the striatum occupied in the 24hr>4hr20m statistical parametric map (SPM) of the normal mice to be a consequence of three factors: 1) continued input from the prefrontal cortex; 2) transfer among striatal interneurons; and 3) feedback along the thalmo-striatal pathway. Likewise, feedback along the thalmo-cortical pathway accounts for highlighted voxels in the retrospinal cortex. We do not observe the pathways (direct or indirect) to the substantia nigra (SNr) or projections to the ventral tegmental area (VTA) in these experiments, implying relatively lower activity of neurons projecting to these locations in the normal mouse.

Both temporal and spatial patterns of Mn^{2+} accumulation in the serotonin transporter knock-out mouse were profoundly different than those observed in the normal mouse. As noted by others, lifelong lack of SERT causes rearrangement of the relative concentrations and distributions of the various serotonin receptors (Gobbi et al., 2001; Holmes et al., 2003; Li et al., 2003; Mathews et al., 2004; Montanez et al., 2003; Murphy and Lesch, 2008) that are thought to lead to a loss of functional integration and inhibitory regulation in neural circuitry related to emotion and effects of drugs of abuse (Hariri and Holmes, 2006; Uhl et al., 2002). Moreover, SERT knock-out mice show changes in dendritic morphology in the PFC (longer apical dendritic branches in the knockout) and the basolateral amygdala (greater neuronal density) (Wellman et al., 2007); as well as significant increases in neuronal cell density in the neocortex (Altamura et al., 2007). Although neurons in the PFC are known to project to the basolateral amygdala (BLA) (Gabbott et al., 2005), no Mn^{2+} transport to the BLA from the injection site in the PFC is seen in the knock-out mouse and only very minor amounts in the normal mouse at 24 hours after injection. We conclude from this that the PFC-BLA circuit is less robust than connections to the more medial structures (CP, ACB, and TH) in both the normal and SERT knock-out mice.

If activity dependent uptake and release are dominant factors determining the Mn^{2+} distribution, then differences in the statistical parametric maps of the normal and SERT knock-out mice likely reflect differences in neuronal circuit activity. At early times, we observed Mn^{2+} accumulation in the CP of SERT knock-outs well before normal mice; indicative of increased activity in the PFC (thus increased Mn^{2+} uptake) and/or more functionally dense connections between the PFC and CP in SERT knock-outs as compared to normal mice. Increased uptake of Mn^{2+} in the PFC of the SERT knock-out is consistent with changes in dendrite morphology and cortical neuronal cell densities observed by others (Altamura et al., 2007; Wellman et al., 2007).

Subsequent connections from the CP to the GP and TH were also found to be more active (and/or denser) in the SERT knock-out versus normal, as evidenced by the occurrence of Mn^{2+} induced intensity increases in GP and TH of the SERT knock-out well before the normal (appearing 2–3 hours post-injection in SERT knock-out versus 3–4 hours post-injection in the normal mice). Although the normal animals are known to have important circuits involving the SNr, VTA, and DNR; no hint of Mn^{2+} transport to these locations was observed in the normal animal. In contrast, at 24 hours post-injection we do note Mn^{2+} accumulation in these

same structures in the SERT knock-out. Thus, one or more of three conditions apply in the SERT knock-out when compared with the normal mouse: 1) increased uptake because of increased activity in neurons projecting from CP/GP to SNr/VTA/DNR and subsequent delivery of Mn^{2+}; 2) more neurons projecting to these areas; and/or 3) increased dendritic uptake by neurons in these areas.

Mn^{2+} labels a well defined subset of the known projections from the PFC. Labeled projections are qualitatively different in normal as compared to SERT knock-out animal. The schematic in Figure 9 shows the three most striking general differences observed between the SERT knock-out and normal mouse: 1) connections from the PFC to the ACB are observed in normal, but not the SERT knock-out; 2) connections from the PFC to the VTA and SNr are observed in the SERT knock-out, but not the normal mouse; 3) connections in the SERT knock-out progress as far posterior as the dorsal nucleus Raphé and PRN, but stop mid thalamus in the normal mouse. Although connections from the VTA to the ACB are well known in the rodent (Carr and Sesack, 2000;Gabbott et al., 2005;Gerfen, 2004;Sesack and Pickel, 1992), they are not observed here in either the normal or knock-out mice. These findings imply that in the SERT knock-out the mesocortical and nigrostriatal pathways are emphasized at the expense of the mesolimbic pathway. Morphological changes noted by others (*e.g.* changes in barrel field density, neuronal density, and dendritic morphology) likely influence the functional responses reported by Mn^{2+} enhanced MRI. Thus, we predict that PFC projections terminating in the SNr, VTA and PRNr will have different morphology in the SERT knock-out compare to the normal mouse: likely greater neuronal and or dendritic spine density.

The limbic cortical-ventral striatopallidal circuitry is intimately involved in addiction, aggression, and affective disorders (Berton and Nestler, 2006; Everitt and Robbins, 2005; Murphy and Lesch, 2008; Nelson and Trainor, 2007; Robbins and Everitt, 2002). The SERT knock-out animal model used here reflects many human traits associated with particular human SLC6A4 variants (Murphy et al., 2004; Murphy et al., 2003; Uhl, 2006). We have employed Mn^{2+} enhanced MRI to investigate descending neuronal projections originating in the most anterior part of this circuit: the prefrontal cortex. Using MRS, TBM, and DTI we observe similar metabolite profiles, gross anatomy, and structural characteristics in both normal and SERT knock-out mice. MRI provides a view of the brain bridging its cellular-molecular and the behavioral aspects. From the mesoscopic view afforded by MRI, we observe that active circuitry originating in the prefrontal cortex in the SERT knock-out is biased towards more posterior areas (substantia nigra, ventral tegmental area, and dorsal nucleus Raphé) directly involved in the reward circuit pointing to specific modulation of this circuit by the altered lifelong serotonin tone. As illustrated in this work, MRI can be used to link the micro level and macro level aspects of animal models of disease; in this case providing important insights into how a specific molecular alteration (SERT knock-out) is manifested in the complicated and critically important cortico-limbic circuit.

Acknowledgments

We thank Mike Tyszka at Caltech for creation and implementation of the DTI routines; and Cornelius Hojatkashani, Ilya Eckstein, Boris Gutman, Natasha Lepore, Igor Yanovsky and Mubeena Mirza at the Laboratory for NeuroImaging at UCLA for invaluable assistance with LONI pipeline and TBM analysis. The project was funded in part by the Beckman Institute, NIH NIGMS GM47368, NINDS NS046810, P20 RR018757 (E.L.B.), NIDA R01DA18184, and NCRR U24 RR021760 Mouse BIRN (R.E.J.)

References

Alexander DC, Pierpaoli C, Basser PJ, Gee JC. Spatial transformations of diffusion tensor magnetic resonance images. IEEE Transactions on Medical Imaging 2001;20:1131–1139. [PubMed: 11700739]

Altamura C, Dell'Acqua ML, Moessner R, Murphy DL, Lesch KP, Persico AM. Altered Neocortical Cell Density and Layer Thickness in Serotonin Transporter Knockout Mice: A Quantitation Study. Cerebral Cortex 2007;17:1394–1401. [PubMed: 16905592]

Aoki I, Tanaka C, Takegami T, Ebisu T, Umeda M, Fukunaga M, Fukuda K, Silva AC, Koretsky AP, Naruse S. Dynamic activity-induced manganese-dependent contrast magnetic resonance imaging (DAIM MRI). Magnetic Resonance in Medicine 2002;48:927–933. [PubMed: 12465100]

Basser PJ. Inferring microstructural features and the physiological state of tissues from diffusion-weighted images. NMR Biomed 1995;8:333–344. [PubMed: 8739270]

Bearer EL, Falzone TL, Zhang X, Biris O, Rasin A, Jacobs RE. Role of neuronal activity and kinesin on tract tracing by manganese-enhanced MRI (MEMRI). Neuroimage 2007a;37:S37–S46. [PubMed: 17600729]

Bearer EL, Zhang X, Jacobs RE. Live imaging of neuronal connections by magnetic resonance: Robust transport in the hippocampal-septal memory circuit in a mouse model of Down syndrome. Neuroimage 2007b;37:230–242. [PubMed: 17566763]

Bengel D, Heils A, Petri S, Seemann M, Glatz K, Andrews A, Murphy DL, Lesch KP. Gene structure and 5′-flanking regulatory region of the murine serotonin transporter. Molecular Brain Research 1997;44:286–292. [PubMed: 9073170]

Berton O, Nestler EJ. New approaches to antidepressant drug discovery: beyond monoamines. Nat Rev Neurosci 2006;7:137–151. [PubMed: 16429123]

Bottomley PA. Spatial localization in NMR spectroscopy in vivo. Annals of the New York Academy of Sciences 1987;508:333–348. [PubMed: 3326459]

Brian Ross SB. Magnetic resonance spectroscopy of the human brain. The Anatomical Record 2001;265:54–84. [PubMed: 11323770]

Canals S, Beyerlein M, Keller AL, Murayama Y, Logothetis NK. Magnetic resonance imaging of cortical connectivity in vivo. Neuroimage 2008;40:458–472. [PubMed: 18222710]

Canli T, Zhao Z, Desmond JE, Kang EJ, Gross J, Gabrieli JDE. An fMRI study of personality influences on brain reactivity to emotional stimuli. Behavioral Neuroscience 2001;115:33–42. [PubMed: 11256451]

Caron MG. Genetic targeting of catecholamine transporters reveal essential roles in neuromodulation, maintenance of homeostasis and psychostimulant action. Biological Psychiatry 1999;45:5S–6S.

Carr DB, Sesack SR. Projections from the Rat Prefrontal Cortex to the Ventral Tegmental Area: Target Specificity in the Synaptic Associations with Mesoaccumbens and Mesocortical Neurons. J Neurosci 2000;20:3864–3873. [PubMed: 10804226]

Choi IY, Lee SP, Guilfoyle DN, Helpern JA. In vivo NMR studies of neurodegenerative diseases in transgenic and rodent models. Neurochemical Research 2003;28:987–1001. [PubMed: 12737523]

Cross DJ, Minoshima S, Anzai Y, Flexman JA, Keogh BP, Kim Y, Maravilla KR. Statistical mapping of functional olfactory connections of the rat brain in vivo. Neuroimage 2004;23:1326–1335. [PubMed: 15589097]

Cudalbu C, Cavassila S, Rabeson H, van Ormondt D, Graveron-Demilly D. Influence of measured and simulated basis sets on metabolite concentration estimates. Nmr in Biomedicine 2007;9999n/a

Dedeoglu A, Choi JK, Cormier K, Kowall NW, Jenkins BG. Magnetic resonance spectroscopic analysis of Alzheimer's disease mouse brain that express mutant human APP shows altered neurochemical profile. Brain Research 2004;1012:60–65. [PubMed: 15158161]

Dong, HW. Allen Reference Atlas - A Digital Color Brain Atlas of the C57Black/6J Male Mouse. John Wiley & Sons, Inc.; Hoboken, NJ: 2008.

Drapeau P, Nachshen DA. Manganese Fluxes and Manganese-Dependent Neurotransmitter Release in Presynaptic Nerve-Endings Isolated From Rat-Brain. Journal of Physiology-London 1984;348:493–510.

Drobyshevsky A, Song S-K, Gamkrelidze G, Wyrwicz AM, Derrick M, Meng F, Li L, Ji X, Trommer B, Beardsley DJ, Luo NL, Back SA, Tan S. Developmental Changes in Diffusion Anisotropy Coincide with Immature Oligodendrocyte Progression and Maturation of Compound Action Potential. J Neurosci 2005;25:5988–5997. [PubMed: 15976088]

Dykstra LA, Bohn LM, Rodriguiz RM, Wetsel WC, Gainetdinov RR, Caron MG. Rewarding properties of cocaine in dopamine/norepinephrine transporter knockout mice. Faseb Journal 2003;17:A205–A205.

Everitt BJ, Robbins TW. Neural systems of reinforcement for drug addiction: from actions to habits to compulsion. Nat Neurosci 2005;8:1481–1489. [PubMed: 16251991]

Fox M, Andrews A, Wendland J, Lesch KP, Holmes A, Murphy D. A pharmacological analysis of mice with a targeted disruption of the serotonin transporter. Psychopharmacology 2007;195:147–166. [PubMed: 17712549]

Gabbott PLA, Warner TA, Jays PRL, Salway P, Busby SJ. Prefrontal cortex in the rat: Projections to subcortical autonomic, motor, and limbic centers. The Journal of Comparative Neurology 2005;492:145–177. [PubMed: 16196030]

Gainetdinov RR, Caron MG. Monoamine transporters: From genes to behavior. Annual Review of Pharmacology and Toxicology 2003;43:261–284.

Gainetdinov RR, Sotnikova TD, Caron MG. Monoamine transporter pharmacology and mutant mice. Trends in Pharmacological Sciences 2002;23:367–373. [PubMed: 12377578]

Gerfen, CR. Basal Ganglia. In: Paxinos, G., editor. The Rat Nervous System. Academic Press; Sydney: 2004. p. 455-508.

Gobbi G, Murphy DL, Lesch KP, Blier P. Modifications of the Serotonergic System in Mice Lacking Serotonin Transporters: An in Vivo Electrophysiological Study. J Pharmacol Exp Ther 2001;296:987–995. [PubMed: 11181933]

Govindaraju V, Young K, Maudsley AA. Proton NMR chemical shifts and coupling constants for brain metabolites. NMR Biomed 2000;13:129–153. [PubMed: 10861994]

Graveron-Demilly D, Diop A, Briguet A, Fenet B. Product operator algebra for strongly coupled spin system. J Magn Reson 1993;A101:233–239.

Groenewegen HJ, Uylings HBM. The prefrontal cortex and the integration of sensory, limbic and autonomic information. Cognition, Emotion and Autonomic Responses: The Integrative Role of the Prefrontal Cortex and Limbic Structures 2000;126:3–28.

Groenewegen HJ, Wright CI, Uylings HBM. The anatomical relationships of the prefrontal cortex with limbic structures and the basal ganglia. Journal of Psychopharmacology 1997;11:99–106. [PubMed: 9208373]

Gruetter R. Automatic, Localized Invivo Adjustment of All 1st-Order and 2nd-Order Shim Coils. Magnetic Resonance in Medicine 1993;29:804–811. [PubMed: 8350724]

Hagen MC, Zald DH, Thornton TA, Pardo JV. Somatosensory processing in the human inferior prefrontal cortex. Journal of Neurophysiology 2002;88:1400–1406. [PubMed: 12205161]

Hall FS, Sora I, Drgonova J, Li XF, Goeb M, Uhl GR. Molecular mechanisms underlying the rewarding effects of cocaine. Current Status of Drug Dependence/Abuse Studies: Cellular and Molecular Mechanisms of Drugs of Abuse and Neurotoxicity 2004:47–56.

Hammers A, Allom R, Koepp MJ, Free SL, Myers R, Lemieux L, Mitchell TN, Brooks DJ, Duncan JS. Three-dimensional maximum probability atlas of the human brain, with particular reference to the temporal lobe. Human Brain Mapping 2003;19:224–247. [PubMed: 12874777]

Hariri AR, Holmes A. Genetics of emotional regulation: the role of the serotonin transporter in neural function. Trends in Cognitive Sciences 2006;10:182–191. [PubMed: 16530463]

Hasan KM, Basser PJ, Parker DL, Alexander AL. Analytical computation of the eigenvalues and eigenvectors in dt-mri. J Magn Reson 2001;152:41–47. [PubMed: 11531362]

Hennig J, Nauerth A, Friedburg H. Rare imaging - a fast imaging method for clinical MR. MagnResonMed 1986;3:823–833.

Hetherington HP, Pan JW, Chu WJ, Mason GF, Newcomer BR. Biological and clinical MRS at ultra-high field. NMR Biomed 1997;10:360–371. [PubMed: 9542734]

Hof, PR.; Bloom, FE.; Belichenko, PV.; Celio, MR. Comparative Cytoarchitectonic Atlas of the C57bl/6 and 129/SV Mouse Brains. Elsevier; New York: 2000.

Holmes A, Li Q, Murphy DL, Gold E, Crawley JN. Abnormal anxiety-related behavior in serotonin transporter null mutant mice: the influence of genetic background. Genes, Brain and Behavior 2003;2:365–380.

Homberg JR, Olivier JDA, Smits BMG, Mul JD, Mudde J, Verheul M, Nieuwenhuizen OFM, Schoffelmeere ANM, Ellenbroeik BA, Clippen E. Characterization of the serotonin transporter knockout rat: A selective change in the functioning of the serotonergic system. Neuroscience 2007;146:1662–1676. [PubMed: 17467186]

Jansen JFA, Backes WH, Nicolay K, Kooi ME. 1H MR Spectroscopy of the Brain: Absolute Quantification of Metabolites. Radiology 2006;240:318–332. [PubMed: 16864664]

Kassubek J, Juengling FD, Kioschies T, Henkel K, Karitzky J, Kramer B, Ecker D, Andrich J, Saft C, Kraus P, Aschoff AJ, Ludolph AC, Landwehrmeyer GB. Topography of cerebral atrophy in early Huntington's disease: a voxel based morphometric MRI study. Journal of Neurology Neurosurgery and Psychiatry 2004;75:213–220.

Kim DK, Tolliver TJ, Huang SJ, Martin BJ, Andrews AM, Wichems C, Holmes A, Lesch KP, Murphy DL. Altered serotonin synthesis, turnover and dynamic regulation in multiple brain regions of mice lacking the serotonin transporter. Neuropharmacology 2005;49:798–810. [PubMed: 16183083]

Kita T, Wagner GC, Nakashima T. Current research on methamphetamine-induced neurotoxicity: Animal models of monoamine disruption. Journal of Pharmacological Sciences 2003;92:178–195. [PubMed: 12890883]

Kochunov P, Lancaster JL, Thompson P, Woods R, Mazziotta J, Hardies J, Fox P. Regional spatial normalization: Toward an optimal target. Journal of Computer Assisted Tomography 2001;25:805–816. [PubMed: 11584245]

Kovacevic N, Henderson JT, Chan E, Lifshitz N, Bishop J, Evans AC, Henkelman RM, Chen XJ. A Three-dimensional MRI Atlas of the Mouse Brain with Estimates of the Average and Variability. Cerebral Cortex 2005;15:639–645. [PubMed: 15342433]

LeBihan D. Molecular diffusion, tissue microdynamics and microstructure. NMR Biomed 1995;8:375–386. [PubMed: 8739274]

Lee EF, Jacobs RE, Dinov I, Loew A, Toga AW. Standard atlas space for C57BL/6J neonatal mouse brain. Anat Embryol 2005;210:245–263. [PubMed: 16228227]

Lepore N, Brun C, Yi-Yu C, Ming-Chang C, Dutton RA, Hayashi KM, Luders E, Lopez OL, Aizenstein HJ, Toga AW, Becker JT, Thompson PM. Generalized Tensor-Based Morphometry of HIV/AIDS Using Multivariate Statistics on Deformation Tensors. Medical Imaging, IEEE Transactions on 2008;27:129–141.

Li Q. Cellular and molecular alterations in mice with deficient and reduced serotonin transporters. Molecular Neurobiology 2006;34:51–65. [PubMed: 17003521]

Li Q, Wichems CH, Ma L, Van de Kar LD, Garcia F, Murphy DL. Brain region-specific alterations of 5-HT2A and 5-HT2C receptors in serotonin transporter knockout mice. Journal of Neurochemistry 2003;84:1256–1265. [PubMed: 12614326]

Lira A, Zhou MM, Castanon N, Ansorge MS, Gordon JA, Francis JH, Bradley-Moore M, Lira J, Underwood MD, Arango V, Kung HF, Hofer MA, Hen R, Gingrich JA. Altered depression-related behaviors and functional changes in the dorsal raphe nucleus of serotonin transporter-deficient mice. Biological Psychiatry 2003;54:960–971. [PubMed: 14625138]

Lyoo IK, Renshaw PF. Magnetic resonance spectroscopy: Current and future applications in psychiatric research. Biological Psychiatry 2002;51:195–207. [PubMed: 11839362]

Ma Y, Hof PR, Grant SC, Blackband SJ, Bennett R, Slatest L, McGuigan MD, Benveniste H. A three-dimensional digital atlas database of the adult C57BL/6J mouse brain by magnetic resonance microscopy. Neuroscience 2005;135:1203–1215. [PubMed: 16165303]

Marjanska M, Curran GL, Wengenack TM, Henry PG, Bliss RL, Poduslo JF, Jack CR Jr, Ugurbil K, Garwood M. Monitoring disease progression in transgenic mouse models of Alzheimer's disease with proton magnetic resonance spectroscopy. Proceedings of the National Academy of Sciences 2005;102:11906–11910.

Mathews TA, Fedele DE, Coppelli FM, Avila AM, Murphy DL, Andrews AM. Gene dose-dependent alterations in extraneuronal serotonin but not dopamine in mice with reduced serotonin transporter expression. Journal of Neuroscience Methods 2004;140:169–181. [PubMed: 15589347]

Mattiello J, Basser PJ, LeBihan D. The b matrix in diffusion tensor echo-planar imaging. MagnResonMed 1997;37:292–300.

Maudsley, AA. Magnetic Resonance Spectroscopic Imaging. In: Toga, AW.; Mazziotta, J., editors. Brain Mapping: The Methods. Academic Press; San Diego: 2002. p. 351-378.

May A, Gaser C. Magnetic resonance-based morphometry: a window into structural plasticity of the brain. Current Opinion in Neurology 2006;19:407–411. [PubMed: 16914981]

Mechelli A, Friston KJ, Frackowiak RS, Price CJ. Structural Covariance in the Human Cortex. J Neurosci 2005;25:8303–8310. [PubMed: 16148238]

Montanez S, Owens WA, Gould GG, Murphy DL, Daws LC. Exaggerated effect of fluvoxamine in heterozygote serotonin transporter knockout mice. Journal of Neurochemistry 2003;86:210–219. [PubMed: 12807440]

Mori S, Itoh R, Zhang JY, Kaufmann WE, van Zijl PCM, Solaiyappan M, Yarowsky P. Diffusion tensor imaging of the developing mouse brain. Magn Reson Med 2001;46:18–23. [PubMed: 11443706]

Morris PG. Magnetic resonance imaging and magnetic resonance spectroscopy assessment of brain function in experimental animals and man. J Psychopharmacol 1999;13:330–336. [PubMed: 10667608]

Murayama Y, Weber B, Saleem KS, Augath M, Logothetis NK. Tracing neural circuits in vivo with Mn-enhanced MRI. Magnetic Resonance Imaging 2006;24:349–358. [PubMed: 16677940]

Murphy DL, Lerner A, Rudnick G, Lesch KP. Serotonin transporter: Gene, genetic disorders, and pharmacogenetics. Molecular Interventions 2004;4:109–123. [PubMed: 15087484]

Murphy DL, Lesch KP. Targeting the murine serotonin transporter: insights into human neurobiology. Nat Rev Neurosci 2008;9:85–96. [PubMed: 18209729]

Murphy DL, Li Q, Engel S, Wichems C, Andrews A, Lesch KP, Uhl G. Genetic perspectives on the serotonin transporter. Brain Research Bulletin 2001;56:487–494. [PubMed: 11750794]

Murphy DL, Uhl GR, Holmes A, Ren-Patterson R, Hall FS, Sora I, Detera-Wadleigh S, Lesch KP. Experimental gene interaction studies with SERT mutant mice as models for human polygenic and epistatic traits and disorders. Genes, Brain and Behavior 2003;2:350–364.

Naressi A, Couturier C, Devos J, Janssen M, Mangeat C, de Beer R, Graveron-Demilly D. Java-based graphical user interface for the MRUI quantitation package. Magma 2001;12:141–152. [PubMed: 11390270]

Narita K, Kawasaki F, Kita H. Mn and Mg influxes through Ca channels of motor nerve terminals are prevented by verapamil in frogs. Brain Res 1990;510:289–295. [PubMed: 2158851]

Nelson RJ, Trainor BC. Neural mechanisms of aggression. Nat Rev Neurosci 2007;8:536–546. [PubMed: 17585306]

Numachi Y, Ohara A, Yamashita M, Fukushima S, Kobayashi H, Hata H, Watanabe H, Hall FS, Lesch KP, Murphy DL, Uhl GR, Sora L. Methamphetamine-induced hyperthermia and lethal toxicity: Role of the dopamine and serotonin transporters. European Journal of Pharmacology 2007;572:120–128. [PubMed: 17673199]

Papadakis N, Xing D, Houston G, Smith J, Smith M, James M, Parsons A, Huang C, Hall L, Carpenter T. A study of rotationally invariant and symmetric indices of diffusion anisotropy. Magnetic Resonance Imaging 1999;17:881–892. [PubMed: 10402595]

Pautler RG, Mongeau R, Jacobs RE. In vivo trans-synaptic tract tracing from the murine striatum and amygdala utilizing manganese enhanced MRI (MEMRI). Magnetic Resonance in Medicine 2003;50:33–39. [PubMed: 12815676]

Paxinos, G. The Rat Nervous System. Vol. 3. Academic Press; Sydney: 2004.

Paxinos, G.; Franklin, K. The Mouse Brain in Stereotaxic Coordinates. Vol. 2. Academic Press; San Diego: 2001.

Perani D, Brambati S, Borroni B, Agosti C, Broli M, Alberici A, Mattioli F, Garibotto V, Cotelli M, Gasparotti R, Scifo P, Alonso R, Binetti G, Cappa S, Padovani A. Voxel Based Morphometry and Diffusion Tensor Imaging in corticobasal degeneration and the relationship with neurological features. Neurology 2005;64:A99–A99.

Persico AM. Serotonin and neurodevelopment: The rodent somatosensory system paradigm. European Neuropsychopharmacology 2004;14:S169–S170.

Persico AM, Altamura C, Calia E, Puglisi-Allegra S, Ventura R, Lucchese F, Keller F. Serotonin depletion and barrel cortex development: Impact of growth impairment vs. serotonin effects on thalamocortical endings. Cerebral Cortex 2000a;10:181–191. [PubMed: 10667986]

Persico AM, Baldi A, Dell'Acqua ML, Moessner R, Murphy DL, Lesch KP, Keller F. Reduced programmed cell death in brains of serotonin transporter knockout mice. Neuroreport 2003;14:341–344. [PubMed: 12634480]

Persico AM, Mengual E, Moessner R, Hall SF, Revay RS, Sora I, Arellano J, DeFelipe J, Gimenez-Amaya JM, Conciatori M, Marino R, Baldi A, Cabib S, Pascucci T, Uhl GR, Murphy DL, Lesch KP, Keller F. Barrel pattern formation requires serotonin uptake by thalamocortical afferents, and not vesicular monoamine release. Journal of Neuroscience 2001;21:6862–6873. [PubMed: 11517274]

Persico AM, Mengual E, Moessner R, Revay RS, Sora I, Arellano J, DeFelipe J, Gimenez-Amaya JM, Conciatori M, Marino R, Baldi A, Cabib S, Pascucci T, Uhl GR, Murphy DL, Lesch KP, Keller F. Barrel pattern formation requires serotonin uptake by thalamocortical afferents, while vesicular monoamine release is necessary for development of supragranular layers. Pflugers Archiv-European Journal of Physiology 2000b;440:R34–R34.

Pfefferbaum A, Sullivan E, Hedehus M, Adalsteinsson E, Lim K, Moseley M. In vivo detection and functional correlates of white matter microstructural disruption in chronic alcoholism. Alcoholism-Clinical and Experimental Research 2000;24:1214–1221.

Puig MV, Celada P, Artigas F. Serotonergic control of prefrontal cortex. Revista De Neurologia 2004;39:539–547. [PubMed: 15467993]

Ratiney H, Sdika M, Coenradie Y, Cavassila S, van Ormondt D, Graveron-Demilly D. Time-Domain Semi-Parametric Estimation Based on a Metabolite Basis Set. NMR Biomed 2005;18:1–13. [PubMed: 15660450]

Reading SAJ, Yassa MA, Bakker A, Dziorny AC, Gourley LM, Yallapragada V, Rosenblatt A, Margolis RL, Aylward EH, Brandt J, Mori S, van Zijl P, Bassett SS, Ross CA. Regional white matter change in pre-symptomatic Huntington's disease: A diffusion tensor imaging study. Psychiatry Research-Neuroimaging 2005;140:55–62.

Reith MEA. Studying monoamine transporters: beyond hypermonoaminaemia. Journal of Neuroscience Methods 2005;143:1–2. [PubMed: 15763131]

Rex DE, Ma JQ, Toga AW. The LONI Pipeline Processing Environment. Neuroimage 2003;19:1033–1048. [PubMed: 12880830]

Robbins TW, Everitt BJ. Limbic-Striatal Memory Systems and Drug Addiction. Neurobiology of Learning and Memory 2002;78:625–636. [PubMed: 12559840]

Rocha BA. Stimulant and reinforcing effects of cocaine in monoamine transporter knockout mice. European Journal of Pharmacology 2003;479:107–115. [PubMed: 14612142]

Rorden C, Brett M. Stereotaxic display of brain lesions. Behavioural Neurology 2000;12:191–200. [PubMed: 11568431]

Rothman DL, Behar KL, Hyder F, Shulman RG. In vivo NMR studies of the glutamate neurotransmitter flux and neuroenergetics: Implications for brain function. Annual Review of Physiology 2003;65:401–427.

Rudin M, Beckmann N, Mir A, Sauter A. In-vivo magnetic-resonance-imaging and spectroscopy in pharmacological research - assessment of morphological, physiological and metabolic effects of drugs. Eur J Pharm Sci 1995;3:255–264.

Saleem KS, Pauls JM, Augath M, Trinath T, Prause BA, Hashikawa T, Logothetis NK. Magnetic resonance imaging of neuronal connections in the macaque monkey. Neuron 2002;34:685–700. [PubMed: 12062017]

Sesack SR, Pickel VM. Prefrontal Cortical Efferents in the Rat Synapse on Unlabeled Neuronal Targets of Catecholamine Terminals in the Nucleus-Accumbens-Septi and on Dopamine Neurons in the Ventral Tegmental Area. Journal of Comparative Neurology 1992;320:145–160. [PubMed: 1377716]

Shattuck DW, Leahy RM. Automated graph-based analysis and correction of cortical volume topology. IEEE Trans Med Imaging 2001;20:1167–1177. [PubMed: 11700742]

Shen HW, Hagino Y, Kobayashi H, Shinohara-Tanaka K, Ikeda K, Yamamoto H, Yamamoto T, Lesch KP, Murphy DL, Hall FS, Uhl GR, Sora I. Regional differences in extracellular dopamine and serotonin assessed by in vivo microdialysis in mice lacking dopamine and/or serotonin transporters. Neuropsychopharmacology 2004;29:1790–1799. [PubMed: 15226739]

Silva AC, Lee JH, Aoki I, Koretsky AP. Manganese-enhanced magnetic resonance imaging (MEMRI): methodological and practical considerations. Nmr in Biomedicine 2004;17:532–543. [PubMed: 15617052]

Simmons JM, Saad ZS, Lizak MJ, Ortiz M, Koretsky AP, Richmond BJ. Mapping Prefrontal Circuits In Vivo with Manganese-Enhanced Magnetic Resonance Imaging in Monkeys. J Neurosci 2008;28:7637–7647. [PubMed: 18650340]

Sled JG, Zijdenbos AP, Evans AC. A nonparametric method for automatic correction of intensity nonuniformity in MRI data. IEEE Trans Med Imaging 1998;17:87–97. [PubMed: 9617910]

Song SK, Sun SW, Ramsbottom MJ, Chang C, Russell J, Cross AH. Dysmyelination revealed through MRI as increased radial (but unchanged axial) diffusion of water. Neuroimage 2002;17:1429–1436. [PubMed: 12414282]

Sora I, Hall FS, Andrews AM, Itokawa M, Li XF, Wei HB, Wichems C, Lesch KP, Murphy DL, Uhl GR. Molecular mechanisms of cocaine reward: Combined dopamine and serotonin transporter knockouts eliminate cocaine place preference. Proceedings of the National Academy of Sciences of the United States of America 2001;98:5300–5305. [PubMed: 11320258]

Soria G, Wiedermann D, Justicia C, Ramos-Cabrer P, Hoehn M. Reproducible imaging of rat corticothalamic pathway by longitudinal manganese-enhanced MRI (L-MEMRI). Neuroimage 2008;41:668–674. [PubMed: 18445533]

Spring S, Lerch JP, Henkelman RM. Sexual dimorphism revealed in the structure of the mouse brain using three-dimensional magnetic resonance imaging. Neuroimage 2007;35:1424–1433. [PubMed: 17408971]

Tkac I, Henry PG, Andersen P, Keene CD, Low WC, Gruetter R. Highly resolved in vivo 1H NMR spectroscopy of the mouse brain at 9.4 T. Magnetic Resonance in Medicine 2004;52:478–484. [PubMed: 15334565]

Tkác I, Staruck Z, Choi IY, Gruetter R. In Vivo 1H NMR Spectroscopy of Rat Brain at 1ms Echo Time. Magnetic Resonance in Medicine 1999;41:649–656. [PubMed: 10332839]

Toga, AW.; Mazziotta, JC., editors. Brain Mapping: The Methods. Vol. 2. Academic Press; San Diego: 2002.

Torres GE, Caron MG. Approaches to identify monoamine transporter interacting proteins. Journal of Neuroscience Methods 2005;143:63–68. [PubMed: 15763137]

Tyszka JM, Readhead C, Bearer E, Pautler R, Jacobs RE. Statistical Diffusion Tensor Histology Reveals Regional Dysmyelination Effects in the Shiverer Mouse Mutant. Neuroimage 2006;2006:1058–1065. [PubMed: 16213163]

Uhl GR. Dopamine transporter: Basic science and human variation of a key molecule for dopaminergic function, locomotion, and parkinsonism. Movement Disorders 2003;18:S71–S80. [PubMed: 14531049]

Uhl GR. Molecular Genetics of Addiction Vulnerability. NeuroRX 2006;3:295–301. [PubMed: 16815213]

Uhl GR, Hall FS, Sora I. Cocaine, reward, movement and monoamine transporters. Molecular Psychiatry 2002;7:21–26. [PubMed: 11803442]

Uhl GR, Lin ZC. The top 20 dopamine transporter mutants: structure-function relationships and cocaine actions. European Journal of Pharmacology 2003;479:71–82. [PubMed: 14612139]

Van der Linden A, Van Camp N, Ramos-Cabrer P, Hoeh M. Current status of functional MRI on small animals: application to physiology, pathophysiology, and cognition. Nmr in Biomedicine 2007;20:522–545. [PubMed: 17315146]

van Doorn A, Bovendeerd PH, Nicolay K, Drost MR, Janssen JD. Determination of muscle fibre orientation using Diffusion-Weighted MRI [published erratum appears in Eur J Morphol 1996 Nov; 34(4):325]. Eur J Morphol 1996;34:5–10. [PubMed: 8743092]

Verma R, Mori S, Shen DG, Yarowsky P, Zhang JY, Davatzikos C. Spatiotemporal maturation patterns of murine brain quantified by diffusion tensor MRI and deformation-based morphometry. Proceedings of the National Academy of Sciences of the United States of America 2005;102:6978–6983. [PubMed: 15860588]

Wellman CL, Izquierdo A, Garrett JE, Martin KP, Carroll J, Millstein R, Lesch KP, Murphy DL, Holmes A. Impaired Stress-Coping and Fear Extinction and Abnormal Corticolimbic Morphology in Serotonin Transporter Knock-Out Mice. J Neurosci 2007;27:684–691. [PubMed: 17234600]

Wieshmann U, Clark C, Symms M, Franconi F, Barker G, Shorvon S. Reduced anisotropy of water diffusion in structural cerebral abnormalities demonstrated with diffusion tensor imaging. Magnetic Resonance Imaging 1999;17:1269–1274. [PubMed: 10576712]

Woods RP, Grafton ST, Holmes CJ, Cherry SR, Mazziotta JC. Automated image registration: I. General methods and intrasubject, intramodality validation. J Comput Assist Tomogr 1998a;22:139–152. [PubMed: 9448779]

Woods RP, Grafton ST, Watson JD, Sicotte NL, Mazziotta JC. Automated image registration: II. Intersubject validation of linear and nonlinear models. J Comput Assist Tomogr 1998b;22:153–165. [PubMed: 9448780]

Xu F, Gainetdinov RR, Wetsel WC, Jones SR, Bohn LM, Miller GW, Wang YM, Caron MG. Mice lacking the norepinephrine transporter are supersensitive to psychostimulants. Nat Neurosci 2000;3:465–471. [PubMed: 10769386]

Yamashita M, Fukushima S, Shen HW, Hall FS, Uhl GR, Numachi Y, Kobayashi H, Sora I. Norepinephrine transporter blockade can normalize the prepulse inhibition deficits found in dopamine transporter knockout mice. Neuropsychopharmacology 2006;31:2132–2139. [PubMed: 16407898]

Zald DH, Mattson DL, Pardo JV. Brain activity in ventromedial prefrontal cortex correlates with individual differences in negative affect. Proceedings of the National Academy of Sciences of the United States of America 2002;99:2450–2454. [PubMed: 11842195]

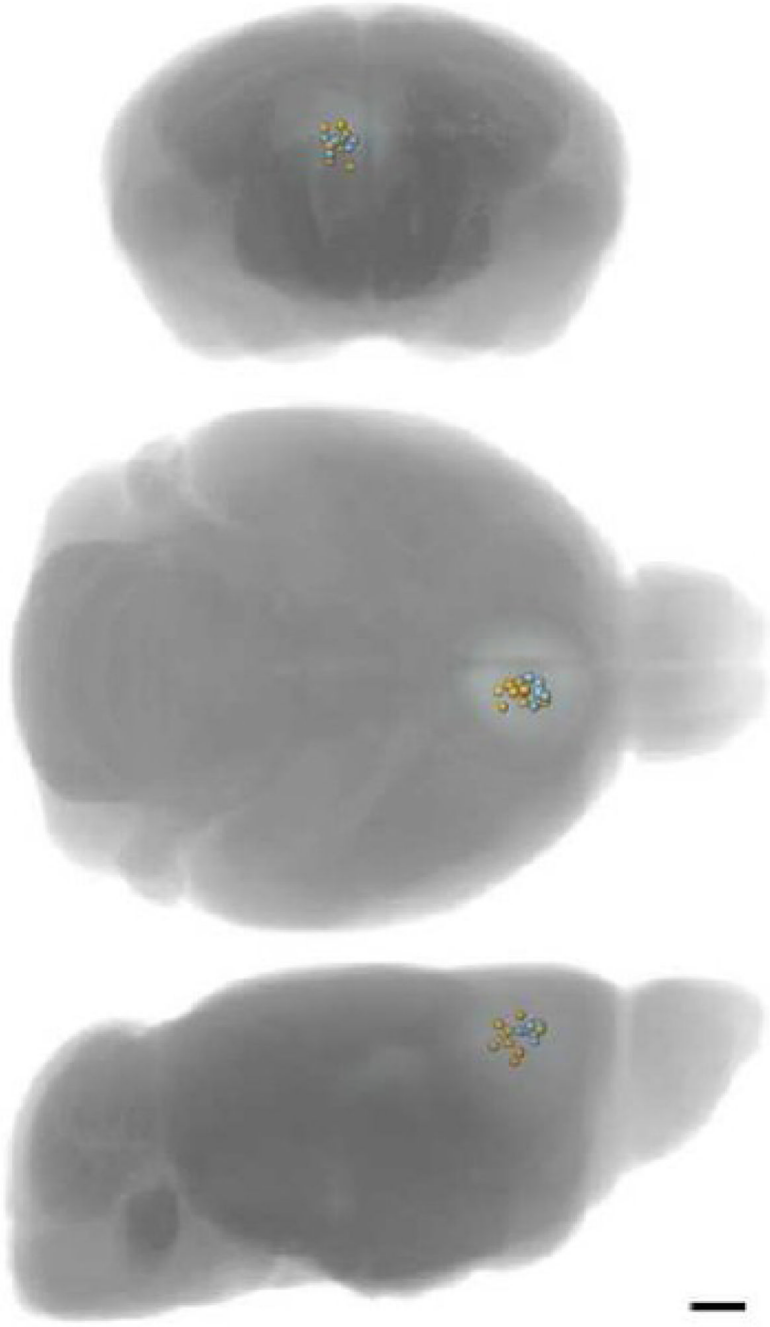

Figure 1. Injection sites are closely grouped within the prefrontal cortex

Location of the injection site is measured as the center of the hypointense region in the MR image recorded 1 hour post–injection. In the three projections, injection sites for individual animals are shown as orange spheres for SERT knock-outs and gray spheres for normal mice. Scale bar = 1mm.

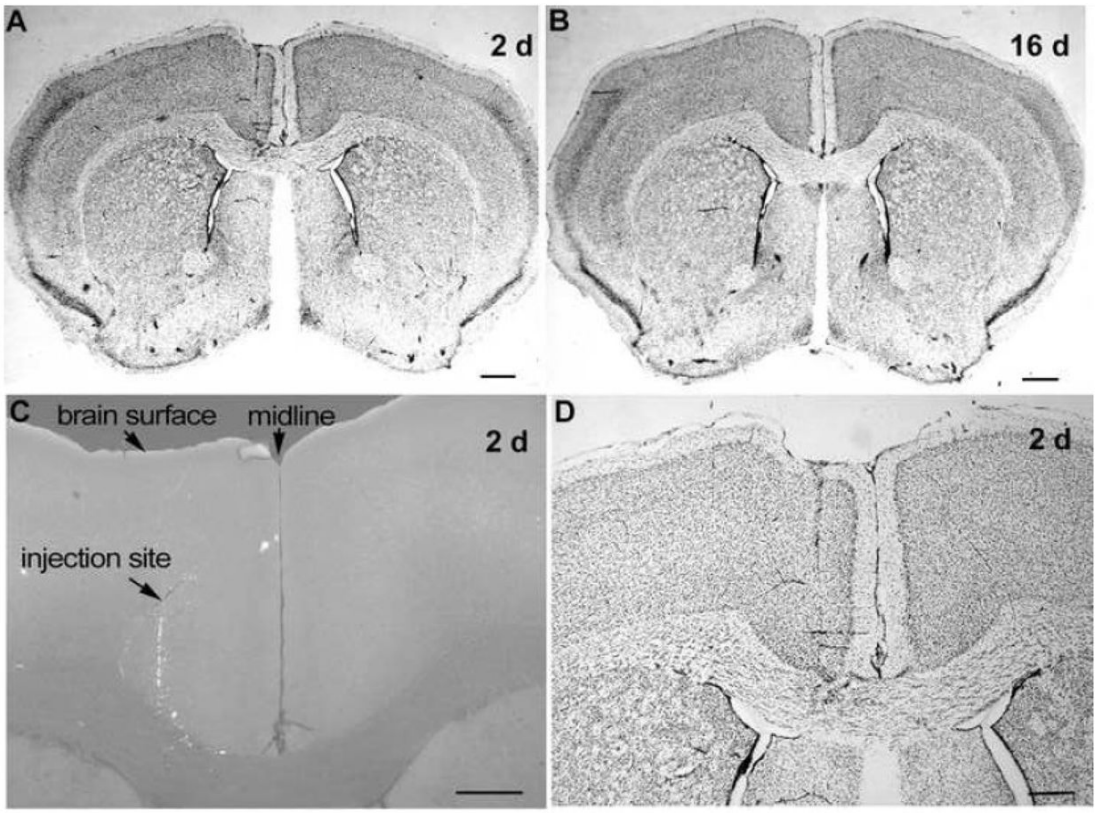

Figure 2. Injection site shows minimal injury

All 20 brains were examined by histology. Examples of a section through the PFC of brains imaged by MR and then fixed for histology, sectioned coronally in the same block in register, and stained in parallel for Nissl/Thionine are shown. The brain in (A) was fixed at 2 days and (B) 16 days after injection. At 2 days (A) an apparent needle track is found in the Nissl/Thionine stained section and confirmed as the injection site in a parallel section imaged by fluorescence (C). The fluorescent tracer has already traveled along neural processes into deeper regions of the brain and along the corpus callosum. Higher magnification (D) reveals no hemorrhage, or evidence of inflammation at the injection site or along the track. At 16 ddays (B) no histologic evidence of the injection can be found nor is any evidence of residual injury detected. Bar = 500μm.

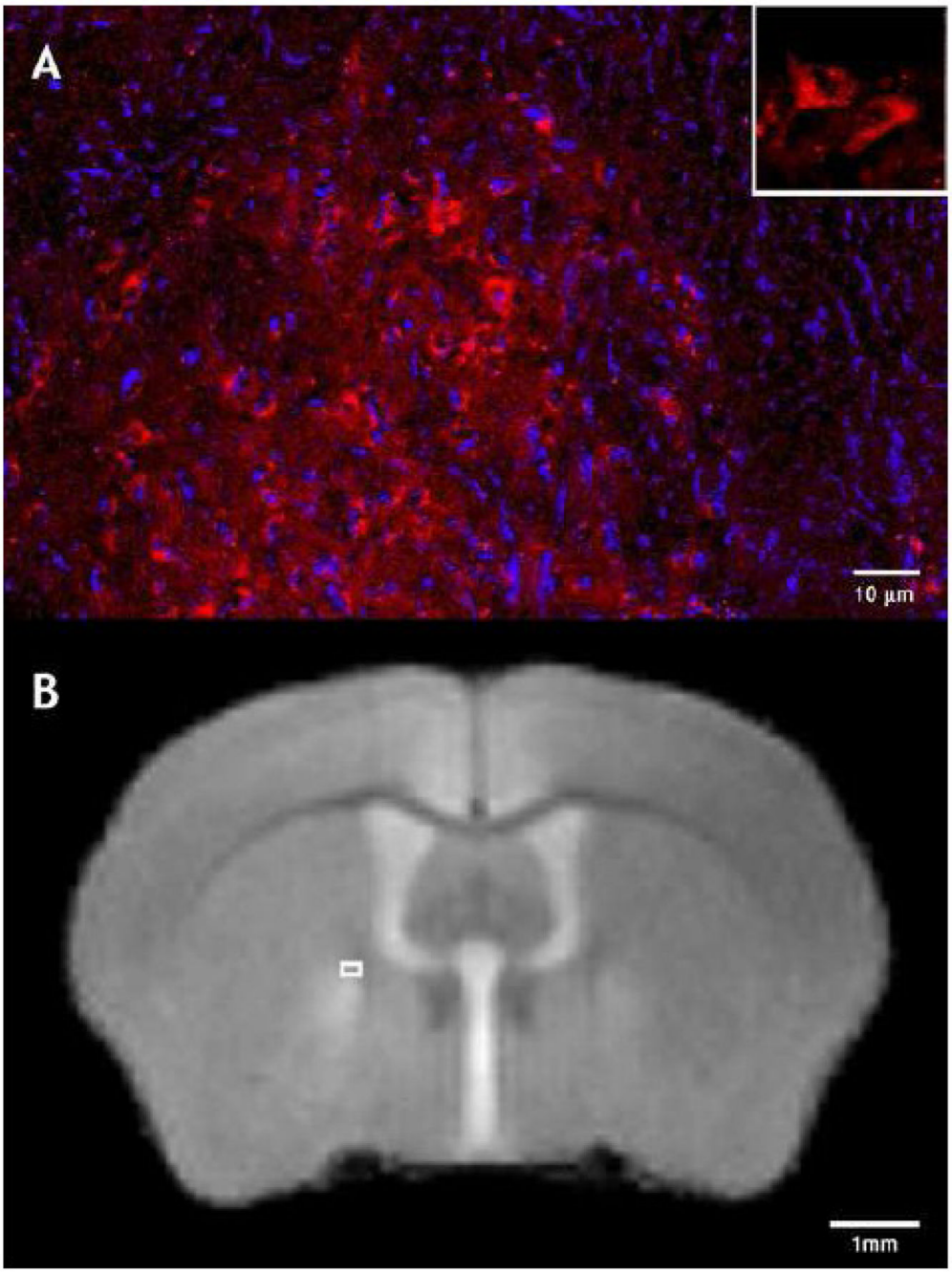

Figure 3. Neuronal transport of rhodamine-dextran and Mn^{2+} overlap in the globus pallidus (GP)

Panel A shows fluorescence microscopy of a coronal section through Bregma −0.3 mm in the GP lateral to the internal capsule. It reveals a cluster of rhodamine-positive neurons ipsilateral to the injection in the same normal mouse as shown in Figure 2A that was co-injected with Mn^{2+} and rhodamine-dextran, imaged by MR and fixed by perfusion 48 hr later. Rhodamine dextran (red) appears as fluorescent particles in the neuronal cell bodies (insert at 2X). Nuclei are stained blue with DAPI. Note the normal neuronal morphology of the dextran-positive cells. Panel B shows the corresponding MR image slice from the 3D data set of the average 24-hour post injection normal mouse that includes the images from the mouse shown in (A).

Note enhanced intensity in the GP. The rectangle in the MR image corresponds to the location and size of fluorescence image in (A).

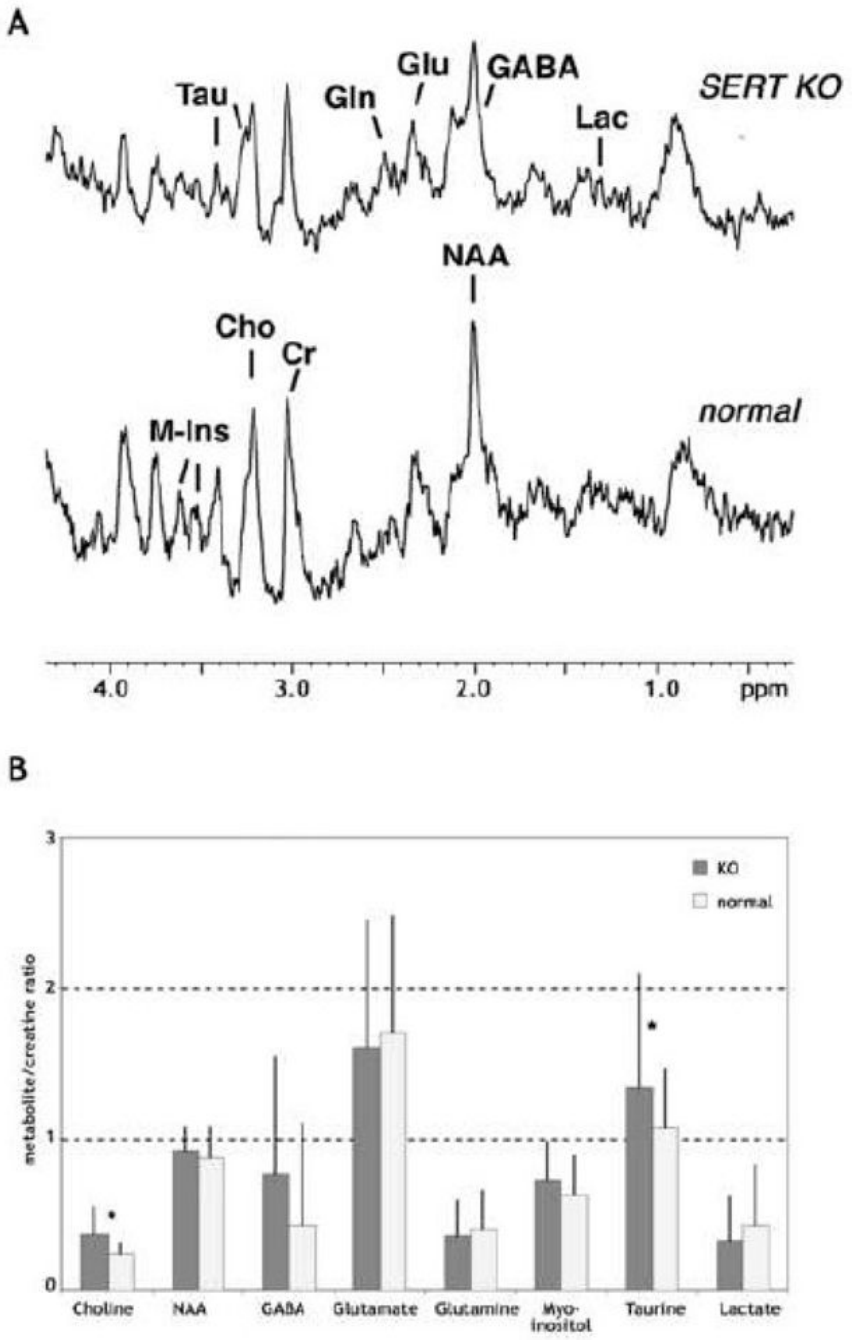

Figure 4. MR spectroscopy detects little difference between SERT knock-out and normal brains

A. Typical *in vivo* proton spectra from a small volume in the striatum reveal good signal-to-noise ratio. Metabolite relative concentrations shown in B are determined from these spectra. B. Metabolite concentrations relative to creatine determined from analysis of *in vivo* spectroscopy data. Only choline and taurine verge on being different in the SERT knock-out (knock-out - shaded bars) versus the normal (normal - unshaded bars) mouse. Student's *t*-test comparison reveals $p<0.054$ (*) for these two metabolites. Only the major peak(s) for each metabolite are noted. Lac: lactate, NAA: N-acetylaspartate, Glu: glutamine, Gln: glutamate, Cr: creatine, Cho: choline, Tau: taurine, GABA: γ-aminobutyric acid, M-Ins: myoinositol.

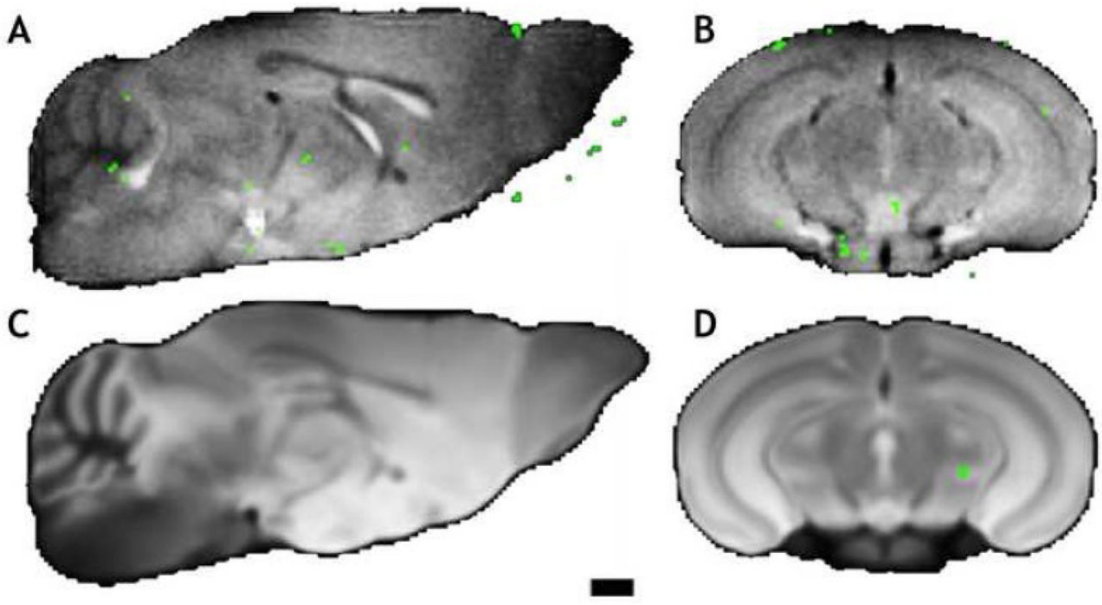

Figure 5. Tensor-based morphometry from in vivo 3D-RARE and isotropic diffusion-weighted MRI data of SERT knock-out and normal mice reveal no meaningful anatomic differences

A and B show para-sagittal and coronal sections, respectively, from the average of all pre-injection 3D RARE in vivo MR scans from both cohorts. C and D show para-sagittal and coronal sections, respectively, from the average of all iDWI *ex vivo* MR scans from both cohorts. Green areas denote those voxels that differ ($p<0.01$) between cohorts in their transformation to the same canonical mouse brain. Scale bar = 1mm.

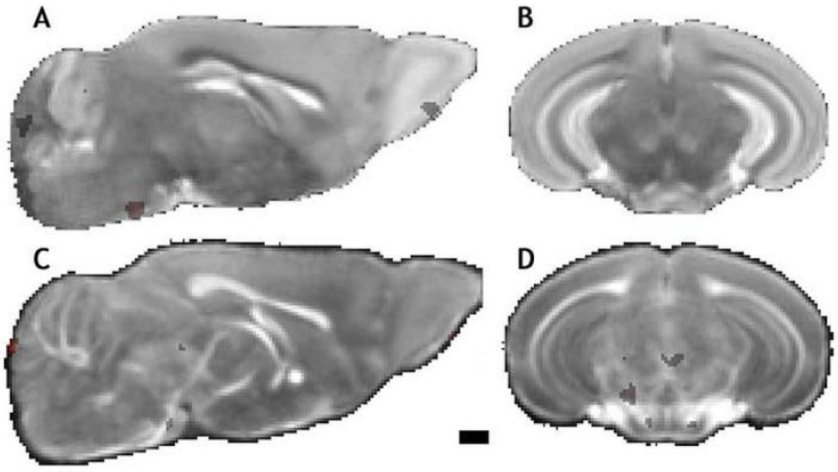

Figure 6. Statistical parametric mapping comparisons of Tr(D) and FA data of SERT knock-out and normal mice exhibit no meaningful differences

A and B show para-sagittal and coronal sections, respectively, from the average of all Tr(D) images derived from *ex vivo* DTI scans from both cohorts. C and D show para-sagittal and coronal sections, respectively, from the average of all FA images derived from *ex vivo* DTI scans from both cohorts. Colored areas show Student's *t*-test comparisons of the FA and Tr (D) values between the two cohorts where red implies SERT knock-out values are greater than normal animal values and blue less. Only $p<0.01$ values are shown and they comprise less than 0.5% of the brain volume. Scale bar = 1mm.

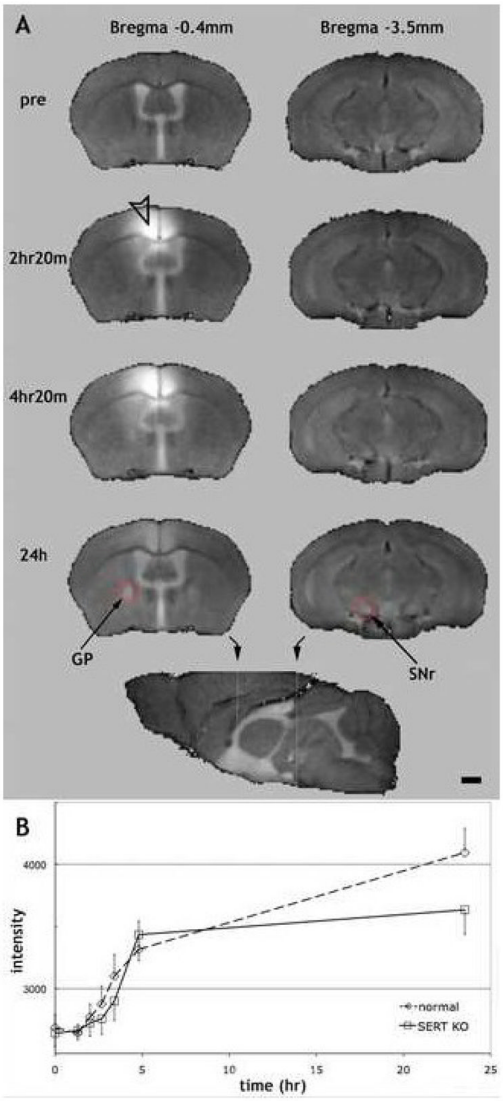

Figure 7. Vizualization of MEMRI shows Mn^{2+} accumulation over time far from the injection site

A. Coronal slices show Mn^{2+} induced hyperintensity near and far from the original injection site. The left and right columns show slices at 0.4mm and 3.5mm posterior to bregma, respectively. Slices are derived from the averaged aligned *in vivo* 3D MR images of 10 SERT knock-out mice. Hyperintensity in the cortex (arrowhead - left column 2nd row) is due to Mn^{2+} passive diffusion from the injection site (Bregma +0.92mm, 0.5mm off midline, 0.9mm from surface), while hyperintensity far from the injection site (*e.g.* GP and SNr) is due to active transport and accumulation. A sagittal slice from the pre-injection image at the bottom notes the locations of the slices. Red circle in the GP notes the location of the center of volume of interest (VOI) used in B. Scale bar =1mm. GP: globus pallidus; SNr: substantia nigra. B. Average intensity in a 0.065μl volume of interest centered in the globus pallidus (red circle in A) increases significantly as a function of time after injection. Squares: SERT knock-out mice; diamonds: normals. Error bars are one standard deviation. Scale bar = 1mm.

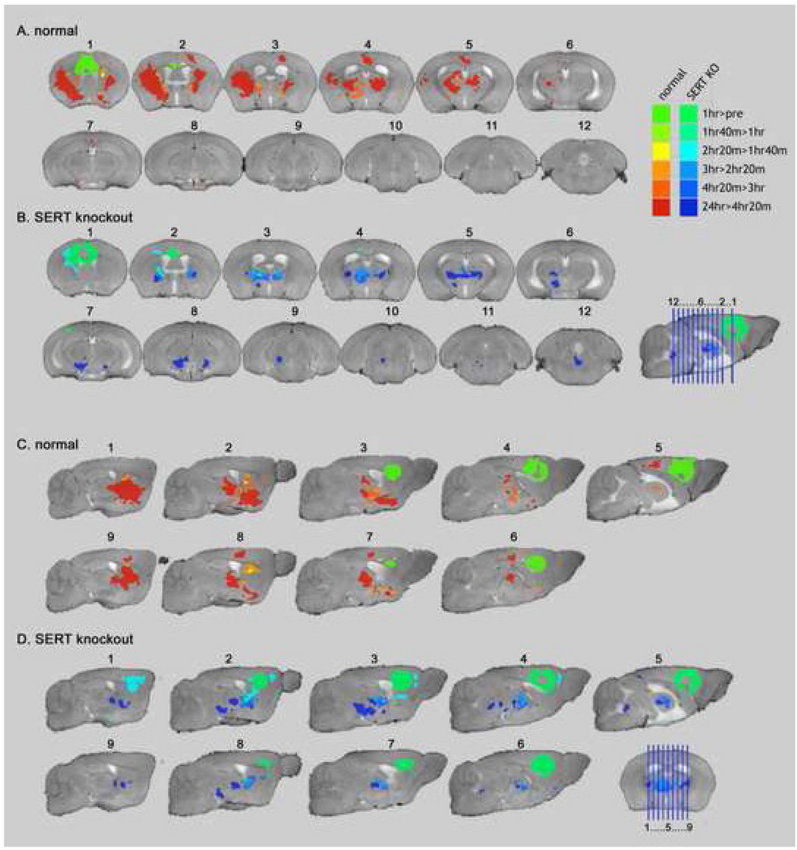

Figure 8. Color-coded statistical parametric maps of the time dependence of Mn^{2+} accumulation after injection in the prefrontal cortex show widespread differences between normal and SERT knock-out mice

A) and B) show coronal slices from normal and SERT knock-out mice, respectively. In both panels coronal slices proceed anterior to posterior from upper left to lower right with placement as shown in the sagittal section. C) and D) show sagittal slices from normal and SERT knock-out mice, respectively. In both panels sagittal slices proceed ipsilateral to contralateral of the injection site with placement as shown in the coronal section. Colored areas denote those regions with significant ($p<0.025$) intensity change between consecutive time points indicating Mn^{2+} tracing to those locations. The 1 hour versus pre-injection comparison is shown in pure green for both the SERT knock-out and normal animals, while later times are displayed with increasing amounts of blue for the SERT knock-out and red for the normal animal. The average pre-injection MR image is show as grayscale background.

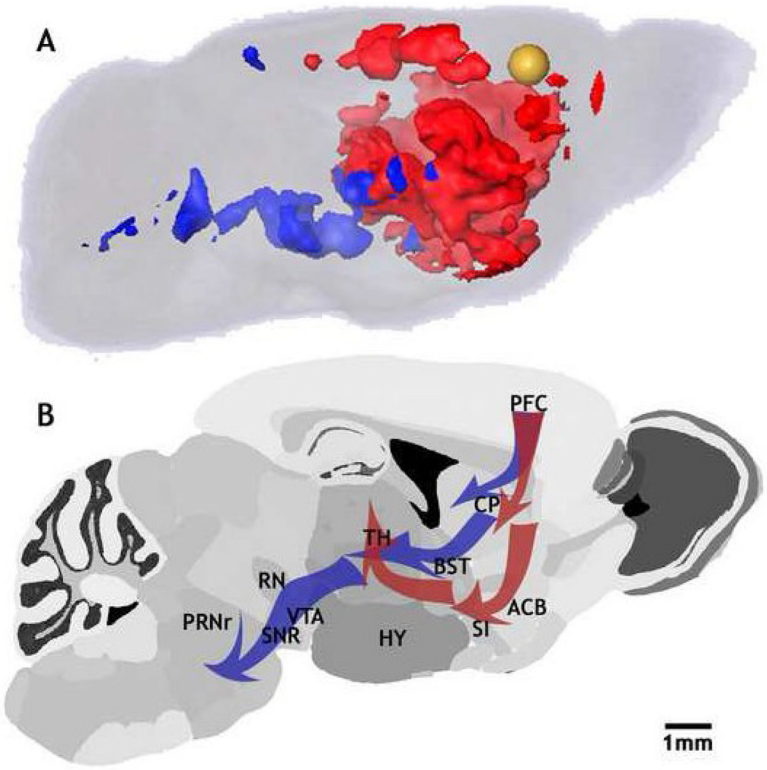

Figure 9. Overview of difference in Mn^{2+} accumulation between SERT knock-out and normal mice

A) Side view of increase in Mn^{2+} hyperintensity at 24hr compared to 4hr20m post injection with normal animals shown in red, SERT knock-out shown in blue, injections site is shown as a brown sphere, and gray semi-transparent background is the average normal animal brain. B) Schematic of circuitry delineated by Mn^{2+} tract tracing shows significant differences between the normal animal and the SERT knock-out. In B) the red arrows denote pathways highlighted in the normal animal, which include the nucleus accumbens (ACB) and extend only as far posterior as the mid thalamus (TH). Blue arrows denote pathways highlighted in the SERT knock-out, which include the ventral tegmental area (VTA) and extend as far posterior as the pontine reticular nucleus (PRNr). Basil nuclei of the stria terminalis: BST; caudate putamen: CP; hypothalamus: HY; prefrontal cortex: PFC; red nucleus: RN; substantia nigra: SNr; substantia innominata: SI.

Table 1

Anatomical features highlighted by Mn^{2+} MRI as a function of time after injection into the prefrontal cortex. Anatomical features were identified by comparing images like those shown in Figure 8 with standard mouse brain atlases ((Hof et al., 2000) and the Allen Brain Atlas (Dong, 2008)). Sagittal sections were typically more helpful than coronal in identifying anatomical structures in the in vivo MR images. KO: SERT knock-out; N: normal control; no subscript: ipsilateral; IC subscript: ipsilateral & contralateral.

	Time after injection when change observed				
Anatomical feature	**1hr**	**1hr40m**	**3hr**	**4hr20m**	**24hr**
PFC: prefrontal cortex	KO & N				
cortex		KO & N			
CP: caudate putamen		KO & N	KO & N_{ic}	KO & N	N_{ic}
GP: globus pallidus		KO	KO_{ic}& N	KO_{ic}	KO & N_{ic}
TH: Thalamus		KO	KO_{ic}	KO & N	KO_{ic} & N_{ic}
ACB: nucleus accumbens			N		N_{ic}
Hypothalamus LHA			KO		
Hypothalamus DMH				N	KO
SI: substantia innominata					N_{ic}
SNr: substania nigra					KO_{ic}
VTA: ventral tegmental area					KO
RN: red nucleus					KO
PRN: pontine reticular nucleus					KO
DNR: dorsal nucleus Raphé					KO

Neuroimage. Author manuscript; available in PMC 2010 July 15.